6. Synchrotron Radiation

Electromagnetic waves propagated in cosmic space derive from a variety of mechanisms. The major contribution in the optical region of the spectrum is from radiation resulting from bound–bound electron transitions between discrete atomic or molecular states, free–bound transitions during recombination, and free–free transitions in the continuum. In the latter case, when $\hbar\omega << kT$ for transitions between levels, radiation classified as *bremsstrahlung* results from the acceleration of electrons traveling in the vicinity of the atom or ion.

In addition, there are other mechanisms of considerable importance operating in the radio region. In particular, there are noncoherent and coherent mechanisms connected with the existence of sufficiently dense plasmas which are responsible for radiation derived from plasma oscillations, such as the sporadic solar radio emissions. This radiation cannot be attributed to the motion of individual electrons in a vacuum but is due to the collective motion of electrons at the plasma frequency

$$\frac{\omega_{pe}}{2\pi} = \frac{1}{2\pi}\sqrt{\frac{n_e e^2}{m_e \varepsilon_0}} = 9\, n_e{}^{1/2} \quad \text{Hz} \tag{6.1}$$

for an electron density n_e (m^{-3}). This often occurs in cosmic plasma when electron beams propagate through a neutralizing plasma background (Section 2.9).

When a plasma is subjected to a magnetic field there is yet another mechanism which plays an extremely important role in radio astronomy. The frequency and angular distribution of the radiation from free electrons moving in the presence of a magnetic field undergoes dramatic changes as the electron energy is increased from nonrelativistic to extreme relativistic energies. Essentially three types of spectra are found. Names such as *cyclotron emission* and *magnetobremsstrahlung* are used to describe the emission from nonrelativistic and mildly relativistic electron energies, whereas the name *synchrotron radiation* is traditionally reserved for highly relativistic electrons because it was first observed in 1948 in electron synchrotrons.

Synchrotron radiation is characterized by a generation of frequencies appreciably higher than the cyclotron frequency of electrons (or positrons) in a magnetic field, a continuous spectra whose intensity decreases with frequency beyond a certain critical frequency, highly directed beam energies, and polarized electromagnetic wave vectors.

In astrophysics, nonthermal (nonequilibrium) cosmic radio emission is, in a majority of cases, synchrotron radiation. This is true for general galactic radio emission, radio emission from the envelopes of supernovae, and radio emission from double radio galaxies and quasars (continuum spectra). Synchrotron radiation also appears at times as sporadic radio emission from the sun, as well as from Jupiter. In addition, optical synchrotron radiation is observed in some instances

(Crab nebula, the radiogalaxy and "jet" in M87–NGC 4486, M82, and others). This apparently is also related to the continuous optical spectrum sometimes observed in solar flares. Synchrotron radiation in the X ray region can also be expected in several cases, particularly from the Crab nebula.

When cosmic radio or optical emission has the characteristics of synchrotron radiation, a determination of the spectrum makes possible a calculation of the concentration and energy spectrum of the relativistic electrons in the emission sources. Therefore, the question of cosmic synchrotron radiation is closely connected with the physics and origin of cosmic rays and with gamma- and X ray astronomy.

Synchrotron radiation was first brought to the attention of astronomers by H. Alfvén and N. Herlofson (1950), a remarkable suggestion at a time when plasma and magnetic fields were thought to have little, if anything, to do in a cosmos filled with "island" universes (galaxies).[1] The recognition that this mechanism of radiation is important in astronomical sources has been one of the most fruitful developments in astrophysics. For example, it has made possible the inference that high-energy particles exist in many types of astronomical objects, it has given additional evidence for the existence of extensive magnetic fields, and it has indicated that enormous amounts of energy may indeed be converted, stored, and released in cosmic plasma.

6.1 Theory of Radiation from an Accelerated Charge

In this section we give, for reference purposes, a series of formulas relating to the energy spectrum of an accelerated charge. For detailed evaluation of the equations the reader is referred to texts such as Panofsky and Phillips (1962).

Consider a charge e in vacuum whose instantaneous position $P'(t')$ is given by the vector $\rho(t')$ and whose instantaneous velocity is $\mathbf{v}(t')$ (Figure 6.1); t' is the time at which the signal propagated at velocity c is emitted at $P'(t')$ to arrive at the position of the observer $P(t)$ at a time t. The "retarded" time t' is related to t through

$$t' = t - \frac{R(t')}{c} \tag{6.2}$$

where $R(t')$ is the distance between e and the observer.

Deriving the electromagnetic fields of the accelerated electron are a straightforward, but lengthy calculation. These are [Jones 1964]

$$\mathbf{E}(r,t) = \frac{e}{4\pi\varepsilon_0}\left[\frac{\left(1-\beta^2\right)\left(\mathbf{n}-\boldsymbol{\beta}\right)}{\left(1-\mathbf{n}\cdot\boldsymbol{\beta}\right)^3 R^2} + \frac{\mathbf{n}\times\left\{\left(\mathbf{n}-\boldsymbol{\beta}\right)\times\dot{\boldsymbol{\beta}}\right\}}{\left(1-\mathbf{n}\cdot\boldsymbol{\beta}\right)^3 cR}\right]_{t'},$$

$$\mathbf{H}(r,t) = \eta\,\mathbf{n}\times\mathbf{E} \tag{6.3}$$

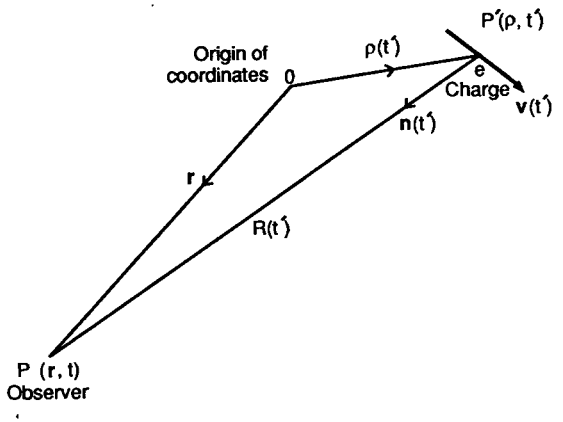

Figure 6.1. Vector diagram of formulation quantities.

where $\eta = \sqrt{\varepsilon_0 / \mu_0}$ is the intrinsic impedance of the propagation medium $\beta = v / c$ and $[\cdots]_{t'}$ denotes that the quantity within the brackets is to be evaluated at the retarded time t' defined by Eq.(6.2). For nonrelativistic motion $\beta \to 0$.

Equation (6.3) consists of two field components. The almost static (induction) near-field can be identified with the first term of Eq.(6.3) which shows it to be independent of the acceleration of the moving charge.[1] The second term of Eq.(6.3) represents the far field or "radiation" field. The far fields **E** and **H** vary linearly with $\boldsymbol{\beta}$, exhibit a $1/R$ fall-off with distance, and are orthogonal to the radius vector. Delineation of the induction and wave zones is given in Figure 6.2.

6.1.1 The Induction Fields

We first consider the importance of the induction field in the problem of radiation from an accelerated charge. In the immediate neighborhood of the charge

$$\mathbf{E} \sim \mathbf{E}_{\text{ind}} = \frac{e}{4\pi\varepsilon_0} \frac{(1-\beta^2)(\mathbf{n}-\boldsymbol{\beta})}{(1-\mathbf{n}\cdot\boldsymbol{\beta})^3 R^2} \tag{6.4}$$

$$\mathbf{H} \sim \mathbf{H}_{\text{ind}} = \mathbf{H}_0 + \eta \frac{e}{4\pi\varepsilon_0} \frac{(1-\beta^2)(\boldsymbol{\beta}\times\mathbf{n})}{(1-\mathbf{n}\cdot\boldsymbol{\beta})^3 R^2} \tag{6.5}$$

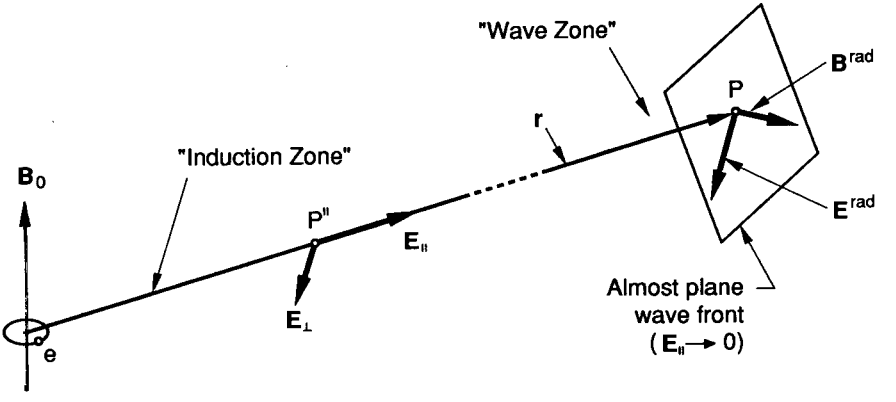

Figure 6.2. Delineation of induction (near-field) and wave (far-field or radiation) zones.

where $\mathbf{H}_0$ is the external magnetic intensity about which the charge spirals. Confining ourselves to the nonrelativistic case, we may then write (for R small in comparison to the radiation wavelength)

$$\mathbf{E}_{\text{ind}} = \frac{e}{4\pi\varepsilon_0}\frac{(\mathbf{n}-\boldsymbol{\beta})}{R^2} \tag{6.6}$$

$$\mathbf{H}_{\text{ind}} = \mathbf{H}_0 + \eta\frac{e}{4\pi\varepsilon_0}\frac{(\boldsymbol{\beta}\times\mathbf{n})}{R^2} \tag{6.7}$$

Neglecting β in Eq.(6.6) leads to

$$\mathbf{E} = \frac{e}{4\pi\varepsilon_0}\frac{\mathbf{n}}{R^2} \tag{6.8}$$

where $\mathbf{n}$ is a unit vector in the direction of R. Thus, we have recovered the electrostatic or Coulomb field. Similarly, since a charge e moving with velocity v is equivalent to an element of current $I\,\mathbf{dl} = e\boldsymbol{\beta}c$, Eq.(6.7) gives

$$d\mathbf{B} = \frac{\mu_0}{4\pi}\frac{I\,d\mathbf{l}\times\mathbf{n}}{R^2} \tag{6.9}$$

Equation (6.9) is simply the Biot–Savart law Eq.(3.5). Thus, the electromagnetic fields generated by an accelerated electron give rise to a strong near-field which can be identified with the Biot–Savart law as-well-as weaker, but propagating, radiation fields. It will be shown that the strong near-fields determine the morphology of the radiating region in a plasma, which is then conveyed to an observer a great distance away via the radiation fields.

6.1.2 The Radiation Fields

The remainder of Sections 6.1 through 6.6 are mainly concerned with the radiation fields. The observation point is assumed to be far away from the charge, so that $\mathbf{n}$ and R change negligibly during a small acceleration interval.

The instantaneous energy flux is given by Poynting's vector

$$\mathbf{S} = \mathbf{E} \times \mathbf{H} = |E|^2 \, \mathbf{n} \tag{6.10}$$

This means that the power radiated per unit solid angle is

$$\frac{\mathrm{d}P(t)}{\mathrm{d}\Omega} = R^2 \, \mathbf{S} \cdot \mathbf{n} = |R \, \mathbf{E}|^2 \tag{6.11}$$

or, in terms of the charge's own time

$$\frac{dP(t')}{d\Omega} = R^2 \, \mathbf{S} \cdot \mathbf{n} \, \frac{dt}{dt'} = \frac{e^2}{16\pi^2 \varepsilon_0 c} \frac{\left| \mathbf{n} \times \left\{ \left(\mathbf{n} - \boldsymbol{\beta} \right) \times \dot{\boldsymbol{\beta}} \right\} \right|^2_{t'}}{\left(1 - \mathbf{n} \cdot \boldsymbol{\beta} \right)^5} \tag{6.12}$$

In deriving Eq.(6.12), the change of variable

$$dt = \frac{\partial t}{\partial t'} dt' = \left(1 - \mathbf{n} \cdot \boldsymbol{\beta} \right) \, dt' \tag{6.13}$$

has been used.

For a nonrelativistic particle, Eq.(6.12) yields

$$\frac{dP(t')}{d\Omega} = \frac{e^2}{16\pi^2 \varepsilon_0 c^3} \left| \mathbf{n} \times \left\{ \mathbf{n} \times \dot{\mathbf{v}} \right\} \right|^2 \tag{6.14}$$

A comparison of Eq.(6.11) and Eq.(6.14) shows that $\mathbf{E}$ lies in the plane containing $\mathbf{n}$ and $\dot{\mathbf{v}}$; when we choose $\dot{\mathbf{v}}$ as the polar axis and Θ as the angle between $\mathbf{n}$ and $\dot{\mathbf{v}}$, it follows that

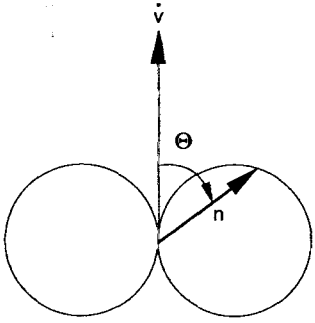

Figure 6.3. Angular distribution of radiation field of a nonrelativistic electron. The pattern is symmetric about the axis $\dot{\mathbf{v}}$.

$$\frac{dP(t')}{d\Omega} = \frac{e^2}{16\pi^2\varepsilon_0 c^3}|\dot{\mathbf{v}}|^2 \sin^2\Theta \tag{6.15}$$

and the polar pattern of the emitted radiation is typically that of an electric dipole (Figure 6.3). This limit is referred to as the *dipole approximation.*

Example 6.1 Total radiation field from an ensemble of charge emitters when $\lambda >> L$. Consider a plasma region of radiating charges of dimension L (Figure 6.4). Let Δt be the time required for an appreciable change in particle motion. If r_c is a characteristic scale of the particle's orbit and v is its velocity, then $\Delta t \sim r_c/\mathrm{v}$. The condition $\Delta t >> L/c$ then implies $\mathrm{v}/c << r_c/L$. Since $r_c < L$, the nonrelativistic condition $\mathrm{v} << c$ is apropos. Under this approximation Eq.(6.3), for a single electron, is

$$\mathbf{E}^{rad}(r,t) = \frac{e}{4\pi\varepsilon_0}\frac{\mathbf{n}\times\langle\mathbf{n}\times\dot{\mathbf{v}}\rangle}{c^2 R} \tag{6.16}$$

For an ensemble of point charges the total radiation field is a linear superposition of the radiated field from each charge emitter

$$\mathbf{E}^{rad}(r,t) = \frac{1}{4\pi\varepsilon_0}\sum_i \frac{e_i}{R_i}\frac{\mathbf{n}\times\langle\mathbf{n}\times\ddot{\mathbf{r}}_i\rangle}{c^2} \tag{6.17}$$

We shall have a need for the electric dipole moment which, by definition [Stratton 1941], is

$$\mathbf{p}^{(1)} = \int \rho(r)\,\mathbf{r}\,dV \tag{6.18}$$

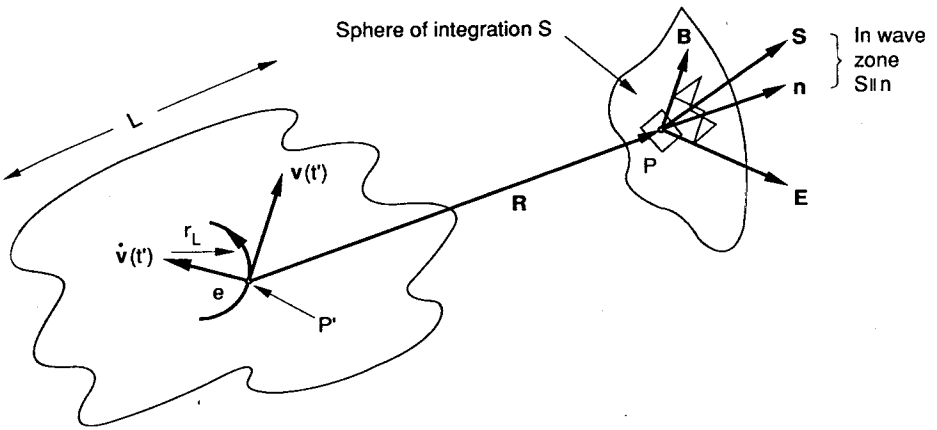

Figure 6.4. Orientation of field vectors from a region L of radiating electrons.

In this notation, the total charge is

$$p^{(0)} = N\,e = \int \rho(r)\,dV \tag{6.19}$$

For N point charges, the electric dipole moment of the distribution Eq.(6.18) is

$$\mathbf{p}^{(1)} = \sum_{i=1}^{N} e_i\,\mathbf{r}_i \tag{6.20}$$

where $\mathbf{r}_i$ are the differential lengths of the dipole elements associated with the emitters e_i. If the variation of the dipole moment is caused by an oscillation, $\mathbf{p}^{(1)} = \sum e_i\,\mathbf{r}_i\,e^{-i\,\omega\,t}$, so that $\sum e_i\,\ddot{\mathbf{r}}_i = -\omega^2\,\mathbf{p}^{(1)}$. Substituting this into Eq.(6.17) and using Eq.(B.7) gives

$$\mathbf{E}^{rad}(r,t) = -\frac{1}{4\pi\varepsilon_0\,R}\,\mathbf{k}\times\{\mathbf{k}\times\mathbf{p}^{(1)}\} \tag{6.21}$$

In deriving Eq.(6.21), use has been made of the fact that in the far-field, $R_i \to R$. The current in the dipole is

$$I = \frac{dq}{dt} = \frac{p^{(1)}}{r_i} = -\frac{i\omega p^{(1)}}{r_i} \tag{6.22}$$

so that $p^{(1)} = I r_i/(-i\omega)$. For a cosinusoidal current distribution aligned along the polar axis, $e\ddot{\mathbf{r}} = -\hat{\mathbf{z}}\omega^2 p\cos\omega t = -\omega^2 \mathbf{p}^{(1)}$, and

$$E^{rad}(r,t) = E_\theta{}^{rad}(r,t) = -k^2 \frac{p\cos\omega t \sin\theta}{4\pi\varepsilon_0 R} \tag{6.23}$$

The total field Eq.(6.3) in the limit $\beta \to 0$, with induction and radiation components, can be cast in terms of the dipole moment [Panofsky and Phillips 1962]:

$$E_R{}^{rad} = \frac{p^{(1)}\cos\theta}{2\pi\varepsilon_0 R^2}\left(\frac{1}{R} - ik\right)e^{ikR} \tag{6.24}$$

$$E_\theta{}^{rad} = \frac{p^{(1)}\sin\theta}{4\pi\varepsilon_0 R}\left(\frac{1}{R^2} - \frac{ik}{R} - k^2\right)e^{ikR} \tag{6.25}$$

$$H_\phi{}^{rad} = \frac{-i\omega p^{(1)}\sin\theta}{4\pi}\left(\frac{1}{R^2} - \frac{ik}{R}\right)e^{ikR} \tag{6.26}$$

The electric fields Eqs.(6.24) and (6.25) can be plotted as a function of space and time and a single time frame of $\mathbf{E}(r,t)$ is shown in Figure 6.5a.

Example 6.2 Radiation from two dipole elements. Consider two oscillating dipole moments $p_1^{(1)}$ and $p_2^{(1)}$ spaced a distance L apart as shown in Figure 6.6. Both oscillate at a frequency ω. The total radiation field seen by an observer is then

$$E_\theta^{rad} = \frac{-k^2}{4\pi\varepsilon_0 R}\left[p_1^{(1)}\cos\omega t + p_2^{(1)}\cos\omega(t-\Delta t)\right]\sin\theta \tag{6.27}$$

where $\Delta t = (\delta/c)\sin\theta$. When $L << \lambda$, Eq.(6.27) is

$$E_\theta^{rad} = \frac{-k^2}{4\pi\varepsilon_0 R}\left(p_1^{(1)} + p_2^{(1)}\right)\cos\omega t \sin\theta \tag{6.28}$$

Figure 6.5b shows the radiation pattern for the case $L = 1/8\ \lambda$. The radiation is now beamed to the upper right. When properly phased, an array of dipole moments will produce a pencil-like beam of radiation.

The total power radiated in all directions is obtained by integrating Eq.(6.12) over the solid angle, with the result, called *Lienard's formula*:

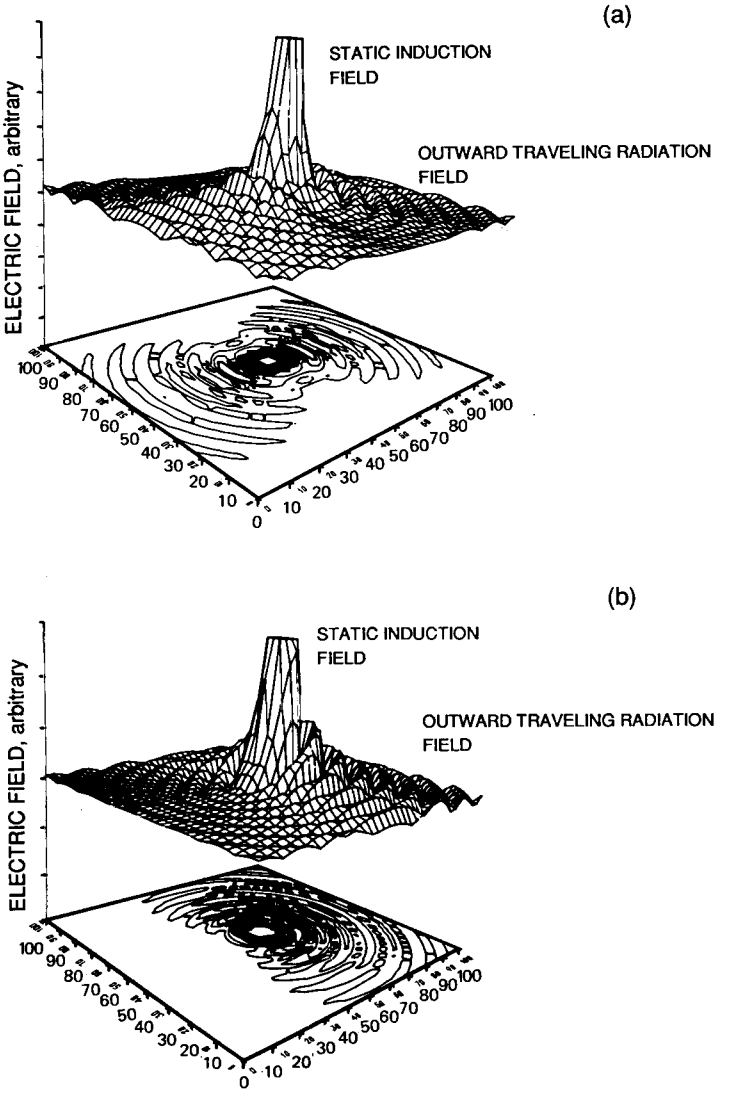

Figure 6.5. Induction and radiation fields E. **(a)** Single dipole radiator, **(b)** two dipoles spaced $\delta = 1/8\ \lambda$ apart. The dipoles are oriented in the plane along axes running from the upper left to the lower right.

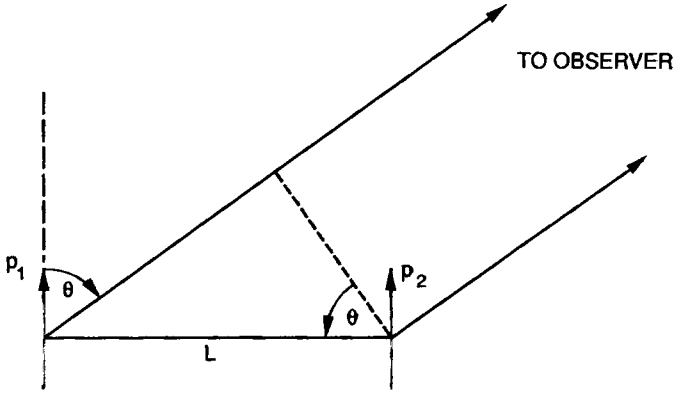

Figure 6.6. Two dipole elements separated by a distance L.

$$P^{\mathrm{T}} = \frac{e^2}{6\pi\varepsilon_0 c}\left[\frac{\dot{\boldsymbol{\beta}}^2 - \left(\boldsymbol{\beta}\times\dot{\boldsymbol{\beta}}\right)^2}{\left(1-\beta^2\right)^3}\right] \tag{6.29}$$

In the dipole approximation Eq.(6.29) reduces to the familiar *Larmor formula* for a nonrelativistic, accelerated charge:

$$P^{\mathrm{T}} = \frac{e^2}{6\pi\varepsilon_0 c^3}|\dot{\mathbf{v}}|^2 \tag{6.30}$$

The total energy radiated is obtained by integrating Eq.(6.30)

$$W_R^T = \int_{-\infty}^{\infty} P^T\,dt = \frac{1}{6\pi\varepsilon_0 c^3}\int_{-\infty}^{\infty}|\dot{\mathbf{v}}(t)|^2\,dt \tag{6.31}$$

To find the frequency spectrum of the radiated energy we Fourier-analyze making use of the Fourier-transform pair

$$V(\omega) = \int_{-\infty}^{\infty} e^{-i\omega t} V(t)\, dt \tag{6.32}$$

$$V(t) = \frac{1}{2\pi} \int_{-\infty}^{\infty} e^{i\omega t} V(\omega)\, d\omega \tag{6.33}$$

and Parseval's theorem for the Fourier components of a function $V(t)$:

$$\int_{-\infty}^{\infty} |V(t)|^2 dt = \frac{1}{\pi} \int_0^{\infty} V(\omega) V^*(\omega) d\omega = \int_0^{\infty} W(\omega) d\omega \tag{6.34}$$

where ω is only defined over positive values, $V(\omega)$ is the Fourier transform of $V(t)$, and $W(\omega)$ defines the spectral energy density. We then find that $W(\omega,\Omega)$ (which has units of joules per unit solid angle per $d\omega$) is

$$W(\omega,\Omega) = \frac{e^2}{16\pi^3 \varepsilon_0 c} \left| \int_{-\infty}^{\infty} e^{i(\mathbf{k}\cdot\boldsymbol{\rho} - \omega t')} \frac{\mathbf{n} \times \{(\mathbf{n} - \boldsymbol{\beta}) \times \dot{\boldsymbol{\beta}}\}}{(1 - \mathbf{n}\cdot\boldsymbol{\beta})^2} dt' \right|^2 \tag{6.35}$$

where t has been transformed to t' by Eq.(6.2) and the large distance $R(t')$ has been approximated by $r - \mathbf{n}\cdot\boldsymbol{\rho}(t')$. Now the unit vector $\mathbf{n}$ is essentially independent of time and points from the origin of coordinates to the point of observation P. Equation (6.35) can be transformed to read

$$W(\omega,\Omega) = \frac{e^2\omega^2}{16\pi^3 \varepsilon_0 c} \left| \int_{-\infty}^{\infty} e^{i(\mathbf{k}\cdot\boldsymbol{\rho} - \omega t')} [\mathbf{n} \times \{\mathbf{n} \times \mathbf{v}\}] dt' \right|^2 \tag{6.36}$$

where this form is obtained by integrating Eq.(6.35) by parts. Note that ω is the frequency measured in the observer's own time scale. The polarization of the radiation is given by the direction of the vector integral of Eq.(6.35) or Eq.(6.36).

6.2 Radiation of an Accelerated Electron in a Magnetic Field

The motion of a particle of charge e and mass m in a uniform static magnetic field $\mathbf{B}_0$ is illustrated in Figure 6.7. The equation of motion Eq.(1.5) is

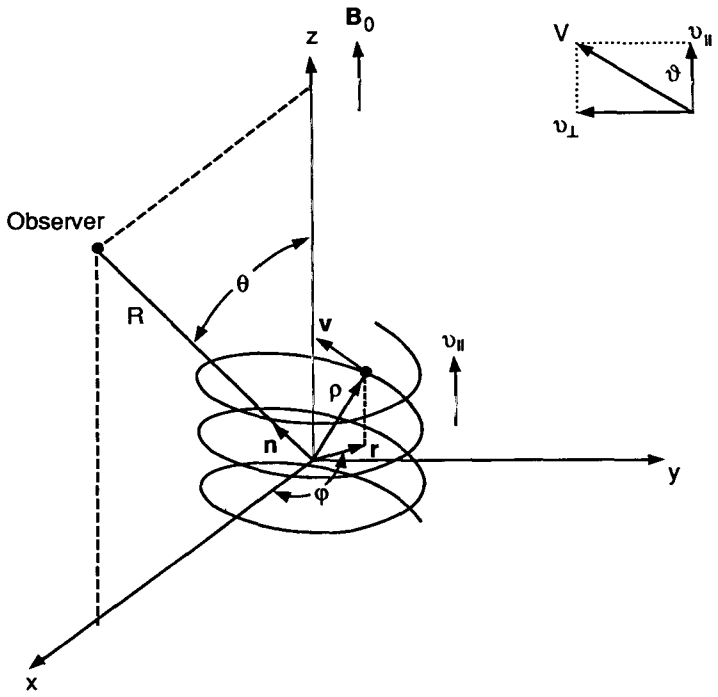

Figure 6.7. Vector diagram for an electron in helical motion in a uniform magnetic field.

$$\frac{d\mathbf{p}}{dt} = e(\mathbf{v} \times \mathbf{B}_0) \tag{6.37}$$

where

$$\mathbf{p} = \gamma m_0 \mathbf{v}, \quad \gamma \equiv \frac{1}{\sqrt{1-\beta^2}} = \frac{W}{mc^2} = \frac{W_{\mathrm{keV}}}{511\mathrm{keV}}, \quad \beta^2 = \left(\frac{v_\parallel}{c}\right)^2 + \left(\frac{v_\perp}{c}\right)^2 \tag{6.38}$$

and $v_\parallel$ and $v_\perp$ are the instantaneous particle velocities along and perpendicular to $\mathbf{B}_0$, respectively. A solution of Eq.(6.37) for the particle velocity v and displacement ρ (e.g., Rose and Clark, Chapter 10) gives

$$\mathbf{v} = \hat{\mathbf{x}}\, v_\perp \cos \omega_\gamma t + \hat{\mathbf{y}}\, v_\perp \sin \omega_\gamma t + \hat{\mathbf{z}}\, v_\parallel \tag{6.39}$$

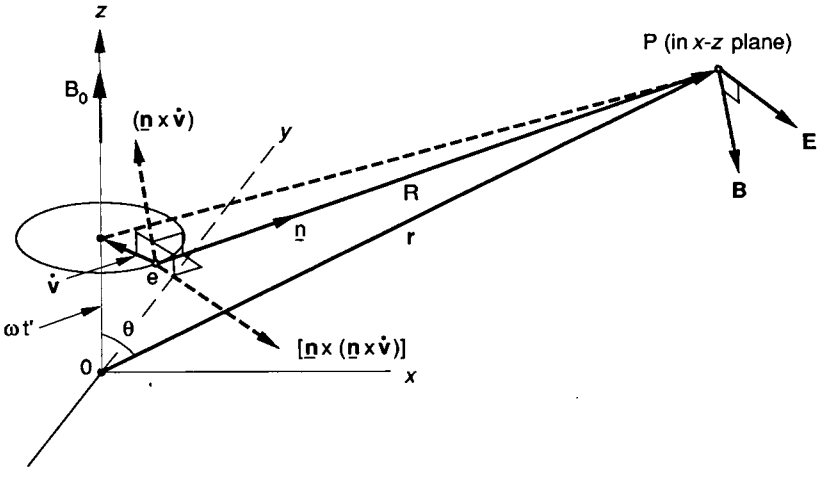

Figure 6.8. Orientation of far-field vectors for an electron in circular motion.

$$\boldsymbol{\rho} = \hat{\mathbf{x}}\,\frac{v_\perp}{\omega_\gamma}\sin\omega_\gamma t - \hat{\mathbf{y}}\,\frac{v_\perp}{\omega_\gamma}\cos\omega_\gamma t + \hat{\mathbf{z}}\,v_\parallel t \tag{6.40}$$

where

$$\omega_b = -\frac{eB_0}{m_0}, \qquad \omega_\gamma = -\frac{eB_0}{m_0\gamma} \tag{6.41}$$

and ω_γ, the relativistic cyclotron frequency, takes account of the relativistic mass charge while ω_b is its value in the limit of zero particle speed. The path of the particle is a circular helix of radius $r = (p_\perp/eB_0)$ and pitch angle ϑ given by $\tan^{-1}\left(2\pi r\omega_\gamma/v_\parallel\right)$. The rotation for an electron is counterclockwise when viewed opposite to the direction of $\mathbf{B}_0$.

From Eq.(6.37) $\dot{\mathbf{v}} \propto \mathbf{v} \times \mathbf{B}_0 \sim \dot{\mathbf{v}}_\perp$, which shows that $\dot{\mathbf{v}}$ is perpendicular to $\mathbf{v}$ (and $\mathbf{B}_0$) with

$$v_\perp = r\omega_\gamma$$

$$\dot{v}_\perp = v_\perp\omega_\gamma \tag{6.42}$$

Figure 6.8 is the circular motion analog of Figure 6.1 and shows the orientation of the radiation field Eq.(6.16). The effect of the parallel motion $v_\parallel$ is a component of the radiation field arising from the motion of the charge along $\mathbf{B}_0$. This is illustrated in Figure 6.9.

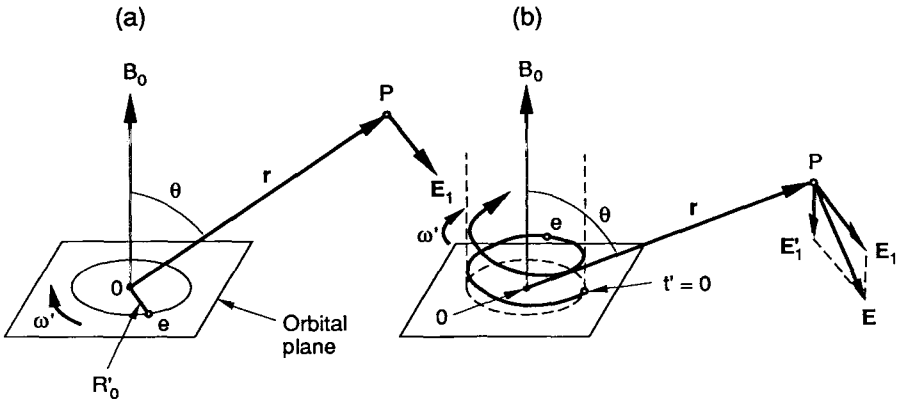

Figure 6.9. Polarization of radiation field E. **(a)** Plane circular orbit. **(b)** Helical orbit.

If the motion is circular so that $v_{\parallel} = 0$ and $v_{\perp} = v$, and if the electron is ultrarelativistic, the electron will be shown to radiate only in the plane of the orbit. An observer located in the plane of rotation would see pulses of radiation corresponding to those instants when the electron is moving precisely towards the observer. The periodicity of the pulses is then

$$T' = \frac{2\pi}{\omega_\gamma} = \frac{2\pi m_0 \gamma}{e B_0} \tag{6.43}$$

The duration of each pulse is [Ginzburg and Syrovatskii 1965]

$$\Delta T' = \frac{m_0}{e B_0} \frac{1}{\gamma^2} \tag{6.44}$$

Figure 6.10 depicts the pulse characteristic for this idealized, single particle case. For the helical motion case when $v_{\parallel} \neq 0$, a pitch angle correction is required in ω_γ. This was first brought out by Epstein and Feldman (1967). For helical motion with pitch angle ϑ (Figure 6.7), the Doppler-shifted time interval between pulses is (Figure 6.11)

$$T_{DS} = T'\left(1 - \beta_{\parallel} \cos \vartheta\right) \approx T'\left(1 - \cos^2 \vartheta\right) \approx T' \sin^2 \vartheta = \frac{2\pi}{\omega_\gamma} \sin^2 \vartheta \tag{6.45}$$

For an ultrarelativistic electron the radiation is very nearly in the direction of its instantaneous motion so that the velocity polar angle $\vartheta \approx \theta$, the coordinate polar angle.

Thus, the radiation field of the electron consists of harmonics of the angular frequency

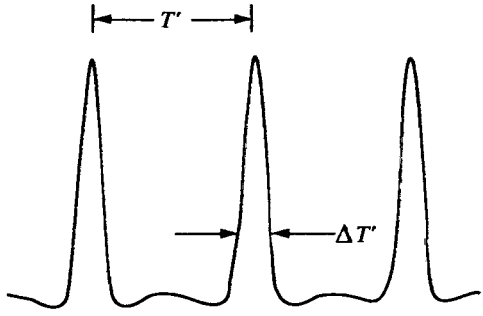

Figure 6.10. Electric field in the wave zone as a function of time for a particle undergoing circular motion in a magnetic field.

$$\omega_{\gamma\, DS} = \frac{2\pi}{T_{DS}} \approx \frac{\omega_\gamma}{\sin^2 \vartheta} \tag{6.46}$$

In the formulation that follows, we shall let $T' \rightarrow T_{DS}$ and $\omega_\gamma \rightarrow \omega_{\gamma DS}$ in order to include the pitch angle correction when the trajectory is helical.

6.2.1 Angular Distribution of the Radiation

The electromagnetic field seen by an observer situated in the radiation zone of Figure 6.2 is periodic with period

$$T = T'\left(1 - \mathbf{n}\cdot\bar{\boldsymbol{\beta}}\right) \tag{6.47}$$

where

$$\bar{\boldsymbol{\beta}} = \frac{1}{T'}\int_{T'} \mathbf{v}(t')/c\; dt' \tag{6.48}$$

From Eq.(6.12), the mean power emitted by the electron per solid angle in the direction $\mathbf{n}$ is defined by

$$\frac{dP}{d\Omega} = R^2 \langle \mathbf{S}\cdot\mathbf{n}\rangle \frac{T}{T'} \tag{6.49}$$

where $< >$ denotes time averaging over the period T. Thus

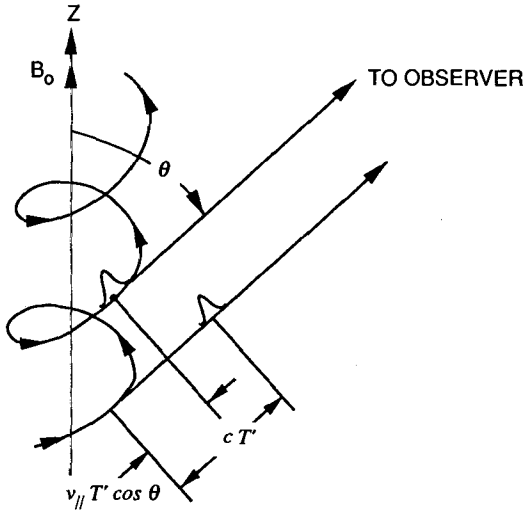

Figure 6.11. Doppler shift of synchrotron radiation emitted by a particle moving towards the observer.

$$\frac{dP}{d\Omega} = \frac{e^2}{16\pi^2\varepsilon_0 c}\frac{1}{T'}\int \frac{\left|\mathbf{n}\times\left[\left(\mathbf{n}-\boldsymbol{\beta}\right)\times\dot{\boldsymbol{\beta}}\right]\right|^2}{\left(1-\mathbf{n}\cdot\boldsymbol{\beta}\right)^5}\,dt' \tag{6.50}$$

Integration of this power over the solid angle gives the total mean power P^T emitted by the electron. Lienard's formula Eq.(6.29) for a periodic velocity motion is then

$$P^T = \frac{e^2}{6\pi\varepsilon_0 c}\frac{1}{T'}\int \frac{\dot{\boldsymbol{\beta}}^2 - \left(\boldsymbol{\beta}\times\dot{\boldsymbol{\beta}}\right)^2}{\left(1-\beta^2\right)^3}\,dt' \tag{6.51}$$

Equation (6.50) reduces to the integral

$$\frac{dP(\theta)}{d\Omega} = \frac{e^2\omega_b^2}{32\pi^3\varepsilon_0 c}\left(1-\beta^2\right)\beta_\perp^2 \times$$

$$\int_0^{2\pi} \frac{\left(\cos\theta-\beta_{//}\right)^2 + \beta_\perp^2\sin^2\theta + 2g_{//}\beta_\perp\sin\theta\sin\phi + \left(1-\beta_{//}^2\right)\sin^2\theta\sin^2\phi}{\left[g_{//}+\beta_\perp\sin\theta\sin\phi\right]^5}\,d\phi \tag{6.52}$$

where $\phi = \omega_\gamma t'$ and $g_\parallel = g_\parallel(\theta) = 1 - \beta_\parallel cos\ \theta$. After integrating [Johner 1988], Eq.(6.52) reduces to

$$\frac{dP(\theta)}{d\Omega} = \frac{e^2\omega_b^2}{32\pi^3\varepsilon_0 c}\left(1-\beta^2\right)\beta_\perp^2\, F(\beta_\parallel, \beta_\perp, \theta) \tag{6.53}$$

where

$$F(\beta_\parallel, \beta_\perp, \theta) = \frac{4g_\parallel^2\left[\left(1-\beta_\parallel^2\right)\left(1-\cos^2\theta\right) - 4\beta_\parallel\cos\theta\right] - \left(1-\beta_\parallel^2+3\beta_\perp^2\right)\beta_\perp^2\sin^4\theta}{4\left(g_\parallel^2 - \beta_\perp^2\sin^2\theta\right)^{7/2}} \tag{6.54}$$

Equation (6.54) reduces to Landau's result [Landau and Lifshitz 1962] when $\beta_\parallel = 0$.

In a way analogous to the directivity of an antenna, the gain $G(\theta)$ is defined as

$$G(\theta) = \frac{dP(\theta)/d\Omega}{P^T_{circular}/4\pi} \tag{6.55}$$

where we have chosen to normalize to the total circular power radiated by an electron. Substituting Eq.(6.42) into Eq.(6.51) while neglecting the time integration gives

$$P^T_{circular} = \frac{e^2\omega_b^2}{6\pi\varepsilon_0 c}\,\frac{\beta_\perp^2}{1-\beta^2} \tag{6.56}$$

From Eqs.(6.53)–(6.56), we get

$$G(\beta_\parallel, \beta_\perp, \theta) = \frac{3}{4}\left(1-\beta^2\right)^2 F(\beta_\parallel, \beta_\perp, \theta) \tag{6.57}$$

The gain $G(\theta)$ is plotted in polar coordinates in Figures (6.12)–(6.14) for various values of $\beta_\parallel$ and $\beta_\perp$. Noteworthy in $G(\theta)$ is the inversion of gain direction between the cases $\beta_\parallel = 0$ as $\beta_\perp$ increases and the essentially forward emission in the relativistic case when $\beta_\parallel/\beta_\perp$ is large.

6.2.2 Frequency Distribution of the Radiation

The energy $W(\omega,\Omega)$ emitted per unit solid angle per frequency interval $d\omega$ is given by Eq.(6.36). To evaluate the exponent appearing in the equation we assume, without loss of generality, that the propagation vector lies in the x–z plane (see Figure B.2). Thus,

$$\mathbf{n} = \hat{\mathbf{x}}\sin\theta + \hat{\mathbf{y}}(0) + \hat{\mathbf{z}}\cos\theta \tag{6.58}$$

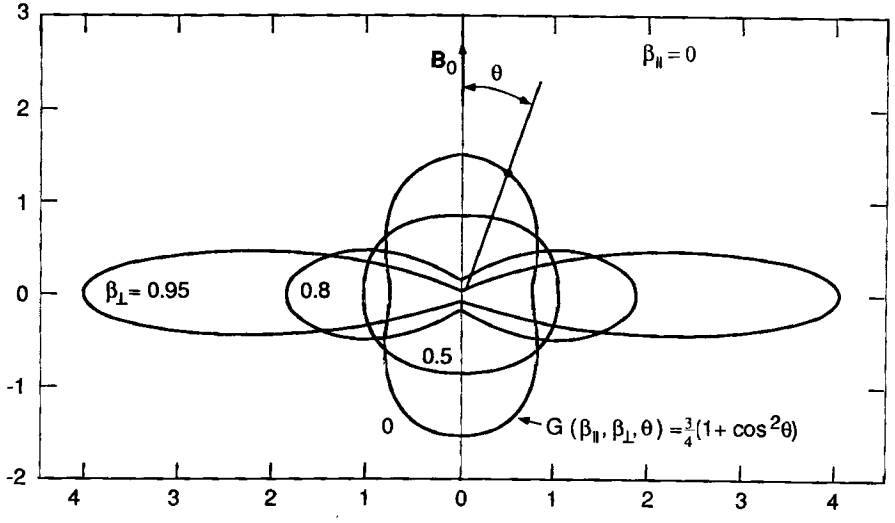

Figure 6.12. Gain patterns for $\beta_{\parallel} = 0$ when $\beta_{\perp} = 0.5$, 0.8, and 0.95.

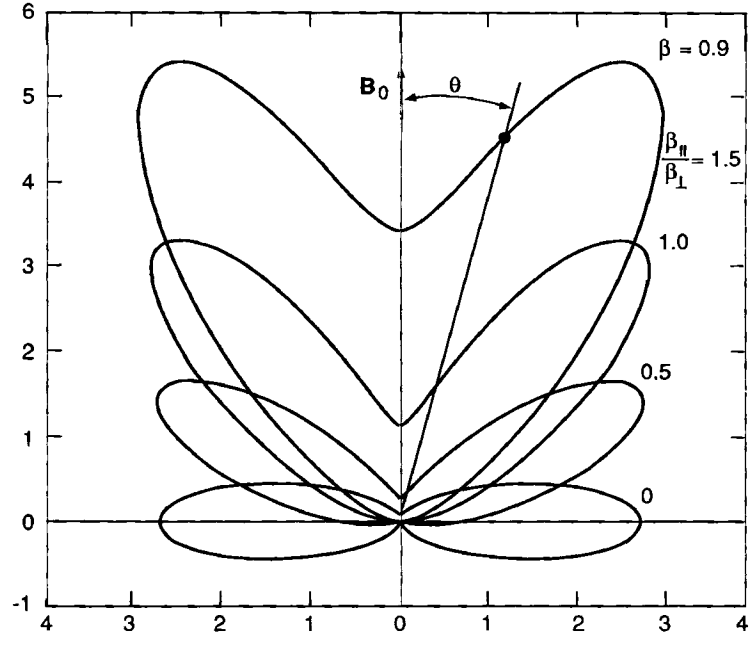

Figure 6.13. Gain patterns for $\beta = 0.9$ and $\beta_{\parallel}/\beta_{\perp} = 0$, 0.5, 1.0, and 1.5.

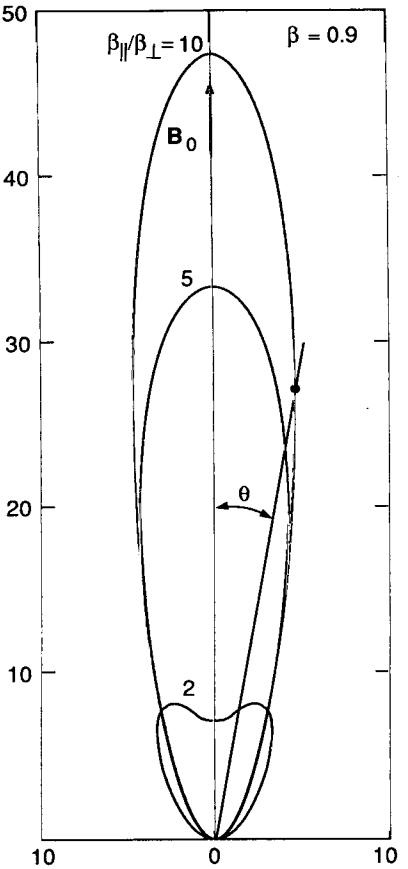

Figure 6.14. Gain patterns for $\beta = 0.9$ and $\beta_\parallel/\beta_\perp = 2$, 5, and 10.

and it follows from Eq.(6.40) that

$$\exp i\left(\mathbf{k}\cdot\boldsymbol{\rho} - \omega t\right) = \exp i\left(\frac{\omega}{\omega_\gamma}\beta_\perp \sin\theta \sin\omega_\gamma t + \omega t\,\beta_\parallel \cos\theta - \omega t\right)$$

$$= \sum_{-\infty}^{\infty} J_m\left(\frac{\omega}{\omega_\gamma}\beta_\perp \sin\theta\right) \exp i\left(m\,\omega_\gamma t + \beta_\parallel\,\omega t\,\cos\theta - \omega t\right) \tag{6.59}$$

(e.g., see Higher Transcendental Functions, Vol.II. Bateman Manuscript Project, p. 7). Substituting Eq.(6.59), the cross product $\mathbf{n} \times (\mathbf{n} \times \mathbf{v})$, and Eq.(B.7) into Eq.(6.36), leads to integrals of the form

$$\int_{-\infty}^{\infty} \left\{1;\ \sin \omega_\gamma t\ ;\ \cos \omega_\gamma t\right\} \exp\left[i\left(x \sin \theta + \omega t \beta_{\|} \cos \theta - \omega t\right)\right] dt \tag{6.60}$$

with solutions

$$2\pi \sum_{-\infty}^{\infty} \left[J_m [x];\ -i \frac{dJ_m [x]}{dx};\ \frac{1 - \beta_{\|} \cos \theta}{\beta_\perp \sin \theta} J_m [x]\right] \delta[y] \tag{6.61}$$

where

$$x = \frac{\omega}{\omega_\gamma} \beta_\perp \sin \theta \tag{6.62}$$

$$y = m \omega_\gamma - \omega\left(1 - \beta_{\|} \cos \theta\right) \tag{6.63}$$

We see that by setting the argument of the delta function in Eq.(6.61) to zero, that the radiation spectrum consists of spectral lines occurring at frequencies

$$\omega = \frac{m \omega_\gamma}{1 - \beta_{\|} \cos \theta} = \frac{m \omega_b \sqrt{1 - \beta_{\|}^2 - \beta_\perp^2}}{1 - \beta_{\|} \cos \theta} \tag{6.64}$$

As shown in Figure 6.11, the term $\beta_{\|} \cos \theta$ ($\propto v_{\|} \cos \theta$) represents the Doppler shift of the observed radiation.

The emitted energy $W(\omega,\Omega)$ is obtained by inserting Eqs.(6.60) and (6.61) in Eq.(6.36). The result has the form $W(\omega,\Omega) = \sum |\cdots|^2 \delta^2(y)$. The emitted power is found by dividing W by the "total time of radiation" given by $\int_{-\infty}^{\infty} \exp(-iyt)\, dt = 2\pi\, \delta(y)$.[1] The quantity obtained is the coefficient of spontaneous emission [Bekefi 1966]

$$P_\omega(\omega, \beta, \theta) = \frac{e^2 \omega^2}{8\pi^2 \varepsilon_0 c} \sum_1^\infty \left| \begin{array}{l} -\hat{x} \dfrac{\cos\theta}{\sin\theta}(\cos\theta - \beta_{\|}) J_m(x) \\ -\hat{y}\, i\beta_\perp \dfrac{dJ_m(x)}{dx} \\ \hat{z}\,(\cos\theta - \beta_{\|}) J_m(x) \end{array} \right|^2 \delta(y) \tag{6.65}$$

The electric field is oriented in the vector direction of Eq.(6.65). The magnitude of Eq.(6.65) is

$$P_\omega(\omega, \beta, \theta) = \frac{e^2 \omega^2}{8\pi^2 \varepsilon_0 c} \left[\sum_1^\infty \left(\frac{\cos\theta - \beta_{\|}}{\sin\theta} \right)^2 J_m^2(x) + \beta_\perp^2 J_m'^2(x) \right] \delta(y) \tag{6.66}$$

In the two foregoing equations the terms of the series $m = 0, -1, -2, \ldots$ were eliminated as not meaningful because of the argument of the delta function.

The total radiation in a given harmonic m is obtained by integrating a single term of the right-hand side of Eq.(6.66) over frequency ω and solid angle $d\Omega = 2\pi \sin\theta d\theta$. The result is [Schwinger 1949];

$$P_m^T = \frac{e^2 \omega_b^2}{2\pi\varepsilon_0 c} \frac{1-\beta_0^2}{\beta_0} \left[m\, \beta_0^2\, J'_{2m}(2m\beta_0) - m^2 (1-\beta_0^2) \int_0^{\beta_0} J_{2m}(2mt)\, dt \right] \tag{6.67}$$

where $\beta_0 = \beta_\perp / \sqrt{1 - \beta_{\|}^2}$. P_m^T, given by Eq.(6.67), is the total emission in all directions, but the emission is anisotropic and depends on the direction of the observer. With the use of Bessel function conversion formulas (Handbook of Mathematical Functions, Dover Publications, 1965), Eq.(6.67) can be written, for the case of relativistic electrons $\gamma >> 1$ and $m >> 1$, as

$$P_m^T = \frac{e^2 \omega_b^2}{4\pi^2 \sqrt{3}\, \varepsilon_0 c} \frac{\beta_0 (1-\beta_0^2)}{\gamma^2} m \left[2K_{2/3}\left(\frac{2m}{3\gamma^3}\right) - \frac{\gamma^2 (1-\beta_0^2)}{\beta_0^2} \int_{2m/3\gamma^3}^\infty K_{1/3}(t)\, dt \right] \tag{6.68}$$

Replacement in Eq.(6.68) of m by ω/ω_γ and then dividing by ω_γ, gives the total emission per unit radian frequency interval rather than per harmonic:

$$P_{\omega}^{T}=\frac{\sqrt{3}\,e^{2}\omega_{b}}{8\pi^{2}\varepsilon_{0}c}\left\{\beta_{0}\left(1-\beta_{0}^{2}\right)\gamma^{2}\frac{\omega}{\omega_{c}}\left[2K_{2/3}\left(\frac{\omega}{\omega_{c}}\right)-\frac{\gamma^{2}\left(1-\beta_{0}^{2}\right)}{\beta_{0}^{2}}\int_{\omega/\omega_{c}}^{\infty}K_{1/3}(t)\,dt\right]\right\} \tag{6.69}$$

where, by definition,

$$\omega_{c}=\frac{3}{2}\omega_{\gamma}\gamma^{3}=\frac{3}{2}\omega_{b}\gamma^{2}$$

$$=2.64\times10^{7}B_{0}(\text{gauss})\left(\frac{W_{\text{keV}}}{511\,\text{keV}}\right)\quad\text{rad/s} \tag{6.70}$$

Figure 6.15 plots the characteristic frequencies versus γ. For example, an electron with $\gamma=10$ (5 MeV) in the presence of a 10^{-4} G field, has a "critical frequency" $\omega_c/2\pi\sim42$ kHz ($\alpha=\pi/2$) whereas a $\gamma=100$ electron (50 MeV) has a "critical frequency" ~4.2 MHz. It will be shown that the critical frequency is located near the frequency at which the spectrum has its maximum value. Otherwise, the "critical frequency" is only a mathematical artifice and has no physical meaning. The actual oscillatory frequency of the gyrating electron $\omega_\gamma/2\pi$ for these two cases is 28 and 2.8 Hz, respectively.

Only for the special case $\beta_{\parallel}=0$ and $\beta_{\perp}\to1$, is the recurrence relation $2K_{2/3}(\xi)+K_{1/3}(\xi)=-K_{5/3}(\xi)$ applicable so that Eq.(6.69) reduces to the well-known circular orbit, highly relativistic synchrotron function

$$P_{\omega}^{T}=\frac{\sqrt{3}\,e^{2}\omega_{b}}{8\pi^{2}\varepsilon_{0}c}\left\{\frac{\omega}{\omega_{c}}\int_{\omega/\omega_{c}}^{\infty}K_{5/3}(t)\,dt\right\} \tag{6.71}$$

The special functions in Eqs.(6.69) and (6.71) are plotted in Figure 6.16.

With the substitution $\omega_\gamma\to\omega_{\gamma DS}$ [Eq.(6.46)], the total radiated power from a single electron at frequency ω [Eq.(6.71)] is divided by the factor $\sin^2\vartheta$. However this factor is cancelled out if we consider the time average of the power emitted from a fixed volume element. Consequently, such a correction is unnecessary for the interpretation of synchrotron emission from radio sources [Scheuer 1968].

The spectrum P_{ω}^{T} for arbitrary $\beta_{\parallel}$ and $\beta_{\perp}$ may be determined by numerically evaluating the $\{\cdots\}$ term in Eq.(6.69). The results of these calculations are shown in Figure 6.17.

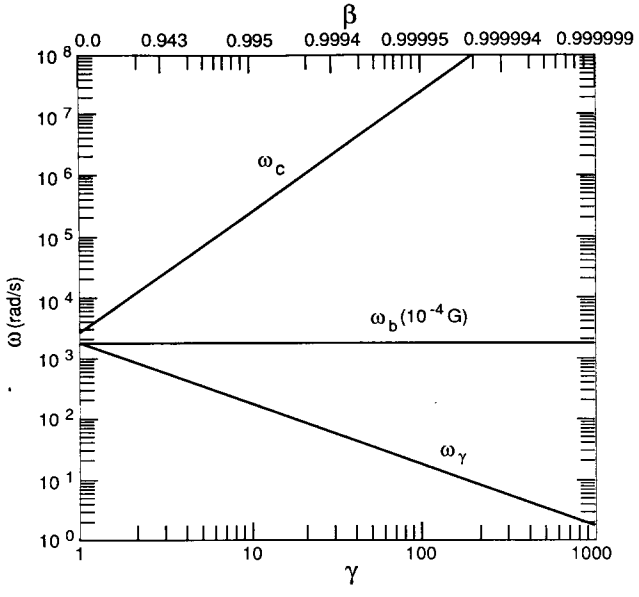

Figure 6.15. The frequencies ω_b, ω_γ, and ω_c vs γ or β.

6.3 Field Polarization

6.3.1 Polarization in the Plane of Rotation

Two independent modes of propagation, ordinary and extraordinary (Appendix B), are identifiable in Eqs.(6.65) and (6.66) when $\theta = \pi/2$. The ordinary mode emissivity component ($\mathbf{E} \parallel \mathbf{B}_0$) is

$$P_\omega^{(O)}(\pi/2) = \frac{e^2\,\omega^2}{8\pi^2\,\varepsilon_0\,c} \sum_1^\infty \beta_\parallel^2\; J_m^2(m\beta_\perp)\;\delta(m\,\omega_\gamma - \omega) \tag{6.72}$$

while the extraordinary mode component ($\mathbf{E} \perp \mathbf{B}_0$) is

$$P_\omega^{(X)}(\pi/2) = \frac{e^2\,\omega^2}{8\pi^2\,\varepsilon_0\,c} \sum_1^\infty \beta_\perp^2\; J_m'^2(m\beta_\perp)\;\delta(m\,\omega_\gamma - \omega) \tag{6.73}$$

The existence of the ordinary wave is due solely to $\beta_\parallel \neq 0$. As shown in Figure B.3, the ordinary wave is linearly polarized along $\mathbf{B}_0$ while the extraordinary wave circumscribes an ellipse in the plane transverse to $\mathbf{B}_0$ as it propagates. Since the angle of propagation (and observation) is

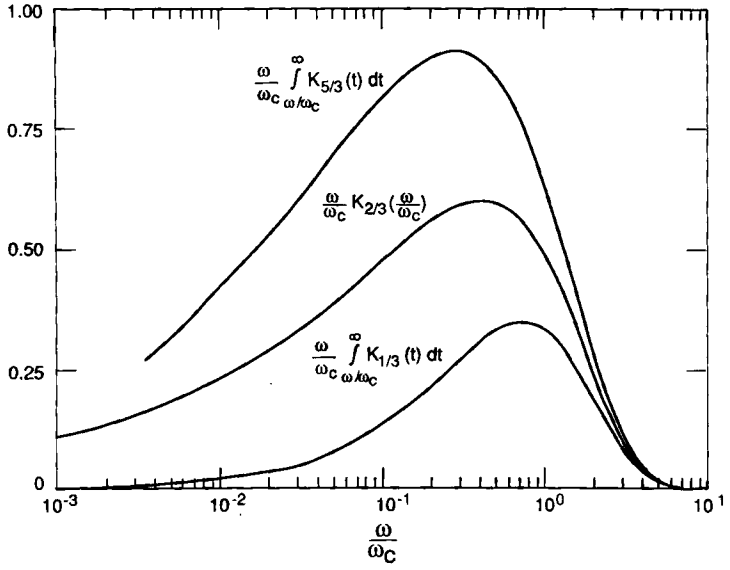

Figure 6.16. Special functions vs ω/ω_c.

$\theta = \pi/2$, Eqs.(6.72) and (6.73) are linearly polarized: $P_\omega^{(O)}$ along $\mathbf{B}_0$ and $P_\omega^{(X)}$ perpendicular to $\mathbf{B}_0$. The Poynting vector Eq.(7.2), and therefore the strength of $P_\omega^{(X)}$, is maximum when $E^{(X)}$ is oriented perpendicular to $\mathbf{n}$.

When $E^{(X)}$ rotates sufficiently to have a component along the line-of-sight, a longitudinal plasma wave $(\mathbf{E}\cdot\mathbf{n} \neq 0)$ exists. The mode conversion properties of an oblique wave propagating in magnetized, nonuniform plasma (i.e., a characteristic of most cosmic plasmas) is beyond the scope of this book and is covered elsewhere [Peratt and Kuehl 1972, Swanson 1989].

6.3.2 Polarization for Arbitrary Angles of Observation

The expression for the power radiated into the m^{th} harmonic in Eq.(6.66) may be written as the sum of two parts,

$$P_\omega(\omega, \beta, \theta) = P_\omega^{(1)} + P_\omega^{(2)} \tag{6.74}$$

where

$$P_\omega^{(1)}(\theta) = \frac{e^2\,\omega^2}{8\pi^2\,\varepsilon_0\,c}\sum_1^\infty \left\{\frac{\cos\theta - \beta_\parallel}{\sin\theta} J_m(x)\right\}^2 \delta(y) \tag{6.75}$$

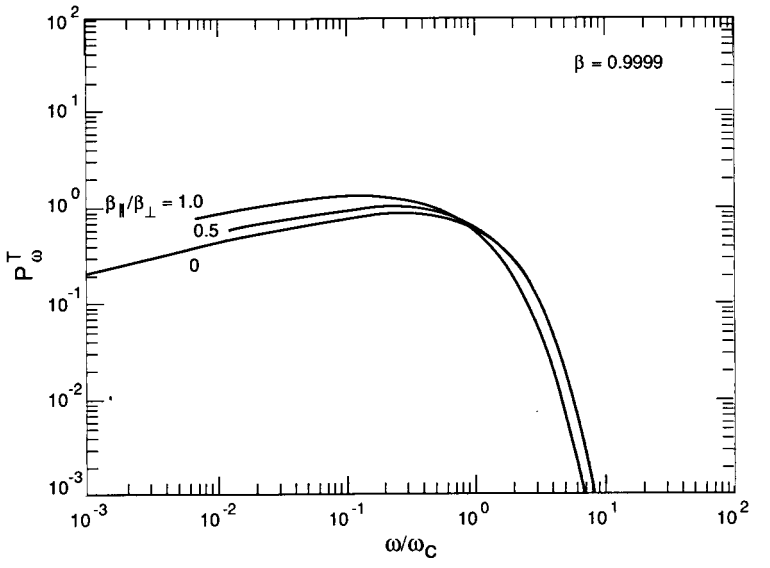

Figure 6.17. Spectrum P_{ω}^{T} vs ω/ω_c for $\beta = 0.9999$ and $\beta_{\|}/\beta_{\perp} = 0$, 0.5, and 1.0.

$$P_{\omega}^{(2)}(\theta) = \frac{e^2\,\omega^2}{8\pi^2\,\varepsilon_0\,c}\sum_{1}^{\infty}\left\{\beta_{\perp}\,J_m'(x)\right\}^2\,\delta(y) \tag{6.76}$$

whose orthogonal field vectors $E_m^{(1)}$ and $E_m^{(2)}$ ($P_{\omega} \sim E_m^2$) lie parallel and perpendicular, respectively, to the projection of $\mathbf{B}_0$ on the plane normal to the line of sight [$\mathbf{B}_0^{\perp \mathbf{n}} = \mathbf{B}_0 - (\mathbf{B}_0 \cdot \mathbf{n})\mathbf{n}$] as shown in Figure 6.18.[2] The easiest way to determine the polarization of the m^{th} harmonic is to take the ratio of the field amplitudes in Eqs.(6.75) and (6.76),

$$R_m = -\frac{E_m^{(1)}}{E_m^{(2)}} = -\left(\frac{\cos\theta - \beta_{\|}}{\beta_{\perp}\sin\theta}\right)\frac{J_m(\psi m)}{J_m'(\psi m)} \tag{6.77}$$

where $\psi = \beta_{\perp}\sin\theta\,/\,(1 - \beta_{\|}\cos\theta)$. The parameter R_m defines the ellipticity of the propagating wave in the direction θ. When $|R_m| = 1$, the wave is circularly polarized while when $R_m = 0$, the wave is linearly polarized. When $0 < R_m < 1$, the wave is elliptically polarized in the ratio of the field amplitudes oriented along the minor and major axes of the ellipse. The polarization of the extraordinary mode rotates in the same sense as does the radiating electron.

Figure 6.19a depicts R_l for the fundamental $m = 1$ mode versus ψ for the case $\theta = \pi/2$. As shown, when $\psi = 0$ ($\theta = \pi/2$), $P_{\omega}^{(1)} = P_{\omega}^{(O)} = 0$, and the existing extraordinary wave is linearly polarized. When $\psi \neq \pi/2$, $P_{\omega}^{(1)}$ is finite and the wave is elliptically polarized.

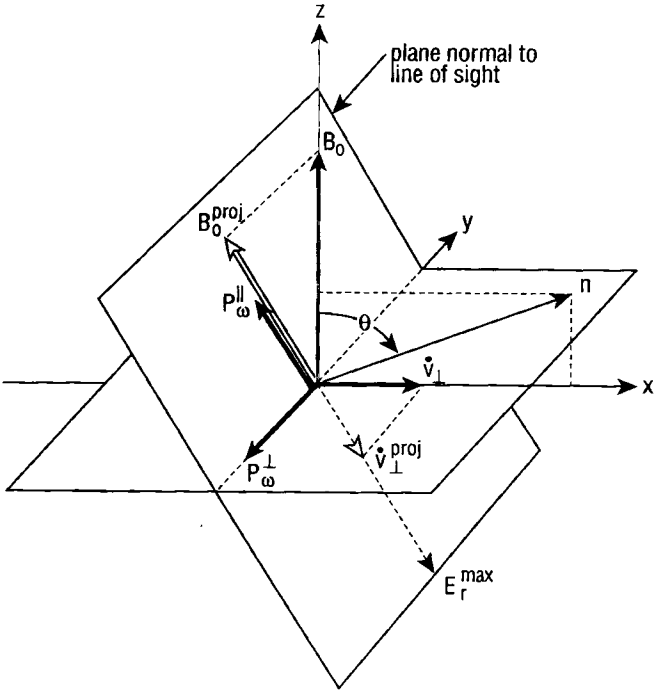

Figure 6.18. Orientation of the quantities $P_\omega^{(\perp)}$ and $P_\omega^{(\parallel)}$.

Figure 6.19b depicts R_m for higher order harmonics as the angle of observation θ is decreased. As shown, the polarization remains more closely circPular over a larger range of ψ when $m >> 1$. A rapid change in the sense of polarization also occurs when $m >> 1$. When $\theta \to 0$, this change occurs for larger values of $\beta_{\parallel}$.

6.4 Radiation from an Ensemble of Electrons

6.4.1 Velocity-Averaged Emissivity

The emissivity averaged over all velocity components is defined by

$$\langle P_\omega^{(2,1)} \rangle = \frac{1}{4\pi} \int_0^\pi P_\omega^{(2,1)} d\beta = \frac{1}{4\pi} \int_0^\pi P_\omega^{(2,1)} (\beta_\perp, \beta_\parallel) 2\pi \sin\vartheta \, d\vartheta \tag{6.78}$$

where $\beta_\parallel = \beta \cos\vartheta$ and $\beta_\perp = \beta \sin\vartheta$.

For the special case $\theta = \pi/2$, Eq.(6.78) can be written as

$$\left\langle P_{\omega}^{(X,O)} \right\rangle = \frac{1}{4\pi} \int_0^{\pi} P_{\omega}^{(X,O)}(\beta_{\perp}, \beta_{\parallel})\, 2\pi \sin\vartheta \, d\vartheta$$

$$= \frac{e^2 \omega^2}{8\pi^2 \varepsilon_0 c} \sum_1^{\infty} A_m^{(X,O)}(\gamma)\, \delta(m\omega_\gamma - \omega) \tag{6.79}$$

where Eqs.(6.72) and (6.73) have been used, and the functions $A_m^{(X,O)}$ embody the pertinent integration over ϑ. Trubnikov (1958) has derived expressions for $A_m^{(X,O)}$ in three distinct energy regimes: nonrelativistic, mildly relativistic, and relativistic,

$$A_m^{(X,O)}(\gamma) = \begin{cases} \dfrac{(m\beta)^{2m}}{(2m+1)!}\left[1\,;\, \dfrac{\beta^2}{2m+3}\right] & m\beta << 1 \\ \dfrac{e^{2m/\gamma}}{\sqrt{16\pi m^3 \gamma}}\left(\dfrac{\gamma-1}{\gamma+1}\right)^m \left[1\,;\, \dfrac{\gamma(\gamma^2-1)}{2m}\right] & \gamma^3 << m \\ \dfrac{1}{4\sqrt{3}\,\pi m \gamma^2}\left[\displaystyle\int_{2m/3\gamma^3}^{\infty} K_{5/3}(t)\, dt \pm K_{2/3}\left(2m/3\gamma^3\right)\right] & \gamma >> 1\,,\ m >> 1 \end{cases} \tag{6.80}$$

Consider the case of relativistic electrons. Because the harmonics are closely spaced in this energy range, the summation in Eq.(6.79) can be replaced by an integration over *dm*. Thus

$$\sum_1^{\infty} A_m^{(X,O)}(\gamma)\, \delta(m\omega_\gamma - \omega) \rightarrow \int_1^{\infty} dm\, A_m^{(X,O)}(\gamma)\, \delta(m\omega_\gamma - \omega)$$

$$= \frac{1}{\omega_\gamma}\left[A_m^{(X,O)}\right]_{m = \omega/\omega_\gamma} \tag{6.81}$$

with the result

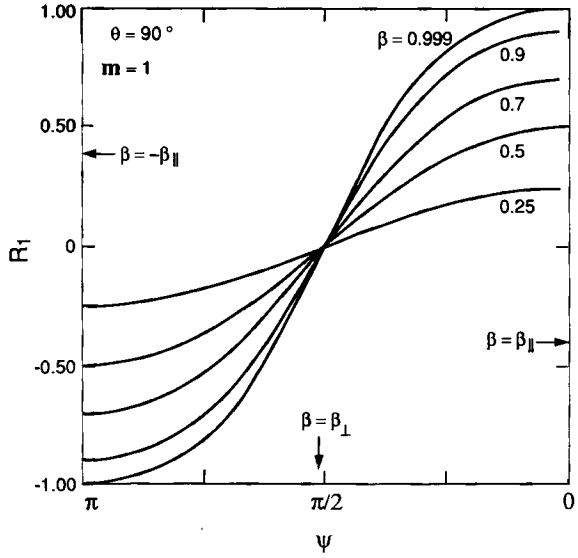

(a)

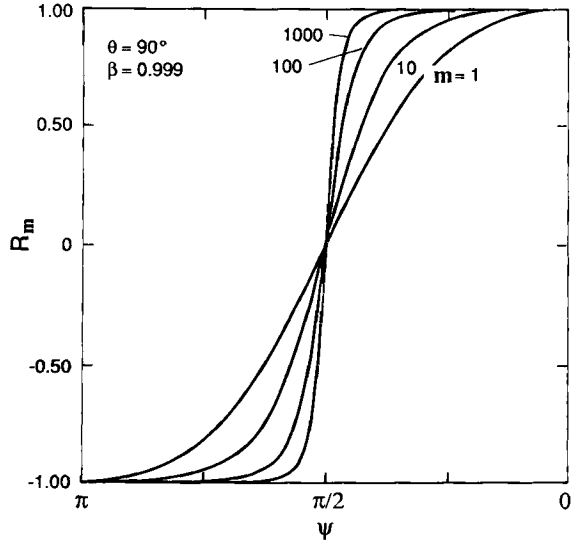

(b)

Figure 6.19. (a) R_t vs ψ for $\theta = 90°$ $\beta = 0.25$, 0.5, 0.7,0.9, and 0.999. (b) R_m vs ψ for $\theta = 90°$, $\beta = 0.999$, for $m = 1$, 10, 100, and 1000. (c) R_m vs ψ for $\theta = 45°$, $\beta = 0.999$, for $m = 1$, 10, 100, and 1000. (d) R_m vs ψ for $\theta = 20°$, $\beta = 0.999$, for $m = 1$, 10, 100, and 1000.

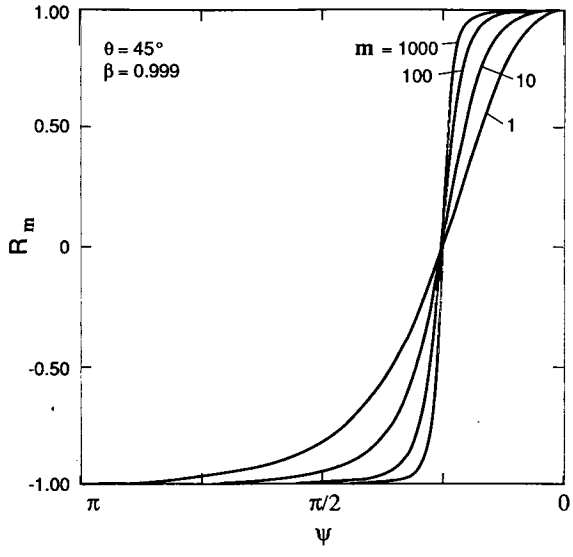
1.00
0.50
0
-0.50
-1.00
R_m
θ = 45°
β = 0.999
m = 1000
100
10
1
π
π/2
0
ψ

(c)

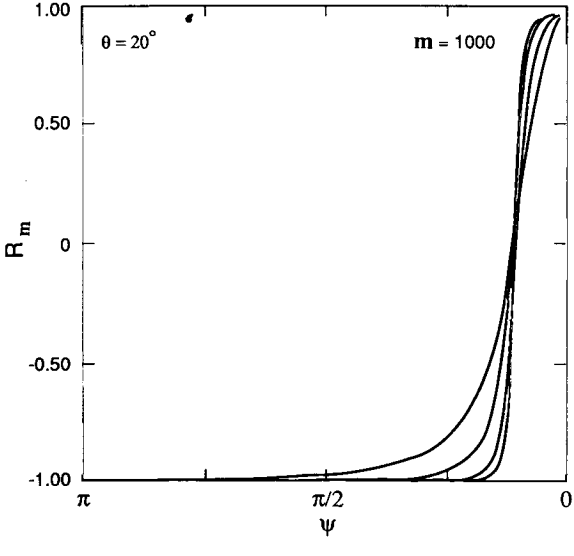
1.00
0.50
0
-0.50
-1.00
R_m
θ = 20°
m = 1000
π
π/2
0
ψ

(d)

$$\langle P_\omega^{(X,O)} \rangle = \frac{\sqrt{3}\, e^2 \omega_b}{64\, \pi^3 \varepsilon_0 c} \left(\frac{\omega}{\omega_c}\right) \left[\int_{2m/3\gamma^3}^{\infty} K_{5/3}(t)\, dt \pm K_{2/3}\left(2m/3\gamma^3\right) \right] \tag{6.82}$$

For arbitrary angles θ, the degree of polarization $\Pi(\theta)$ may be defined as

$$\boxed{\Pi(\theta) = \left| \frac{\langle P_\omega^{(1)} \rangle - \langle P_\omega^{(2)} \rangle}{\langle P_\omega^{(1)} \rangle + \langle P_\omega^{(2)} \rangle} \right|} \tag{6.83}$$

where, in general, the superscripts 1 and 2 denote two independent modes of propagation at angle θ. For $\theta = \pi/2$, the two independent modes of propagation are the ordinary and extraordinary waves. Substituting Eq.(6.82) into Eq.(6.83) gives

$$\Pi(\pi/2) = \left| \frac{\langle P_\omega^{(O)} \rangle - \langle P_\omega^{(X)} \rangle}{\langle P_\omega^{(O)} \rangle + \langle P_\omega^{(X)} \rangle} \right| = \left| \frac{K_{2/3}(\omega/\omega_c)}{\int_{\omega/\omega_c}^{\infty} K_{5/3}(t)\, dt} \right| \tag{6.84}$$

Figure 6.20 shows Eq.(6.83) and Eq.(6.84) versus ω/ω_c for various angles of θ. As shown, the maximum degree of polarization is obtained when $\theta = \pi/2$, when the difference between the amplitudes of the orthogonal modes is maximum. For this case, $\Pi \sim 1/2$ for $\omega/\omega_c << 1$ and $\Pi \sim 1$ for $\omega/\omega_c >> 1$. For oblique angles of observation the degree of polarization falls rapidly for $\omega/\omega_c > 1$. However, for oblique angles the independent modes can no longer be delineated into purely ordinary and extraordinary components.

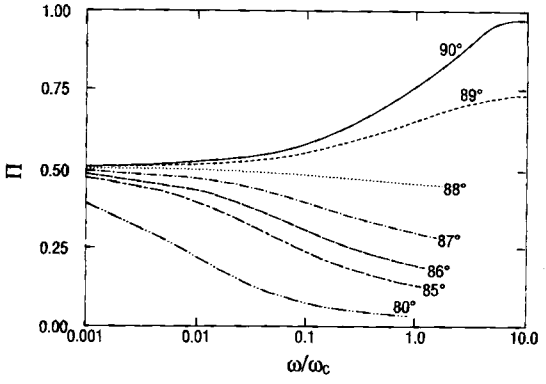

Figure 6.20. Polarization factor Π vs ω/ω_c.

6.4.2 Emission from an Ensemble of Electrons

We now wish to determine the total power radiated by all electrons which have a Maxwellian distribution of energies. First, the emission coefficient j_ω is defined as the sum P_ω over an ensemble of electrons,

$$j_\omega^{(2,\,1)} = \int_0^\infty \left\langle P_\omega^{(2,\,1)} \right\rangle f(p)\, d^3p = \int_0^\infty \left\langle P_\omega^{(2,\,1)} \right\rangle f(p)\, 4\pi\, p^2\, dp \tag{6.85a}$$

The total emission j_ω^T associated with Eq.(6.85a) is

$$j^T = \int_0^\infty P^T(p) f(p)\, 4\pi\, p^2\, dp \tag{6.85b}$$

where $P^T(p)$ is the total emissivity integrated over all frequencies. Substituting Eq.(6.42) into Eq.(6.29) gives

$$P^T(\mathrm{v}) = \frac{e^4 B^2 \mathrm{v}_\perp^2}{6\pi\, \varepsilon_0\, m^2\, c^2 \left(1 - \mathrm{v}^2 / c^2\right)} \tag{6.86}$$

or, in terms of momentum,

$$P^T(p) = \frac{e^4 B^2 p_\perp^2}{6\pi\, \varepsilon_0 m^4 c^3} \tag{6.87}$$

Since $f(p)$ is isotropic and since there are two directions associated with $p_\perp$, but only one associated with $p_\parallel$, we have

$$p_\perp^2 = 2\,\overline{p^2}/3 \tag{6.88}$$

The Maxwellian distribution function is

$$f(p) = C_p \exp\left(-W / kT\right) \tag{6.89}$$

where

$$W = \left(p^2 c^2 + m^2 c^4\right)^{1/2} = \gamma mc^2 \tag{6.90}$$

is the total energy of the particle. The normalization constant can be found from the requirement that

$$\int_0^\infty f(p)\, 4\pi p^2\, dp = C_p \int_0^\infty \exp\left\{-\frac{mc^2}{kT}\left[1 + (p/mc)^2\right]^{1/2}\right\} 4\pi p^2\, dp = 1 \tag{6.91}$$

This integral can be evaluated by setting $\xi = \sqrt{1 + (p/mc)^2}$ and using the Hankel function $H_1^{(1)}(\xi)$, the derivative relation for these functions, and the definition of the modified Bessel function $K_2(\xi)$. We find

$$C_p = \left[4\pi\, kT\, m^2 c\;\; K_2(mc^2/kT)\right]^{-1} \tag{6.92}$$

Finally, from Eqs.(2.2), (6.85b), (6.87), (6.89), and (6.92),

$$j^T = \frac{e^4 B^2 [K_2]^{-1}}{9\pi\, \varepsilon_0\, m^6\, c^4\, kT} \int_0^\infty p^4 \exp\left\{-\frac{mc^2}{kT}\left[1 + (p/mc)^2\right]^{1/2}\right\} dp \tag{6.93}$$

which reduces to

$$\boxed{j^T = \frac{e^4 B^2}{3\pi\, \varepsilon_0\, m^2\, c}\left(\frac{n_e\, kT_e}{mc^2}\right)\frac{K_3(mc^2/kT_e)}{K_2(mc^2/kT_e)}} \quad \mathrm{W/m^3} \tag{6.94}$$

Equation (6.94) is the total power radiated by all the electrons which have a relativistic Maxwellian distribution of energies. A more practical expression may be obtained by expanding the modified Bessel functions in a power series, so that

$$j^T = \frac{e^2\, \omega_b^2}{3\pi\, \varepsilon_0\, c}\left(\frac{n_e\, kT_e}{mc^2}\right)\left(1 + \frac{5}{2}\frac{kT_e}{mc^2} + \ldots\right)$$

$$= 6.2 \times 10^{-17}\, B^2\, (\mathrm{Tesla})\, n_e\, (\mathrm{m^{-3}})\, T_{\mathrm{keV}}\left[1 + T_{\mathrm{keV}}/204\ \mathrm{keV} + \ldots\right] \quad \mathrm{W/m^3} \tag{6.95}$$

More restrictively, if the radiating filaments are in a thermal/magnetic pressure balance, so that from Eq.(8.20) $\beta_p = 2\mu_0 n_e k(T_e + T_i)/B^2 = 1$, then Eq.(6.95) becomes

$$j^T = 5.0 \times 10^{-38}\, n_e^2\, (\mathrm{m^{-3}})\, T_{\mathrm{keV}}^2\left[1 + T_{\mathrm{keV}}/204\ \mathrm{keV} + \ldots\right] \quad \mathrm{W/m^3} \tag{6.96}$$

From either Eq.(6.95) or Eq.(6.96), the total radiated power $j^T V$ over a volume V can be computed.

6.5 Synchrotron Radiation from Z Pinches

Charged particle beams held together or pinched by their self-magnetic fields have been of general interest since their earliest investigation by Bennett (1934). Confinement in the simple cylindrical pinch is a result of the axial, or z, directed current I_z; hence, the name "Z" or "*zed*" pinch, often used in place of *Bennett pinch*. The macroscopic picture of such a beam is that of a self-consistent magnetic confinement or compression against the expansion due to thermal pressure Eq.(1.9). On the microscopic scale, the individual particle orbits include radial oscillations due to the Lorentz force Eq.(1.5) superimposed on the drift in the direction of mean flow. Since they imply particle acceleration, there is electromagnetic radiation associated with them. Because the force is a $\mathbf{v}\times\mathbf{B}$ force, the radiation from the relativistic electrons is synchrotron radiation.

Manifestations of the pinch effect appear to the laboratory observer as a rapidly occurring phenomena. A burst of radiation from high-current discharges (with current densities of the order 10^{11}A/cm^2), such as low-inductance vacuum sparks, plasma focus devices, and exploded wires, is found over a broad spectral range: the microwave region to the hard X ray region. Recorded data show that the radiation bursts are correlated with dips in the current waveform. The microwaves observed are attributed to the synchrotron radiation of electrons in the magnetic field of the proper current. The hard X ray quanta are attributed to synchrotron radiation from the electrons at the transitions between Landau levels in this same current-induced magnetic field [Meierovich 1984].

This phenomena may be similar to that of impulsive solar microwave bursts which are believed to be produced by the synchrotron radiation of electrons accelerated in solar flares [Takakura 1960, 1963, Kawabata 1964, 1965, Kai 1965, Ramaty 1972].

Z pinches as sources of synchrotron radiation in the laboratory have been studied by Meierovich (1984) and by Newberger (1984), who used the Los Alamos PHERMEX Facility. PHERMEX produces a 30 MeV ($\gamma \sim 57$), 1 kA electron beam that is synchrotron-loss limited in energy. Like the sun, which generates synchrotron radiation and solar radio outbursts at microwave frequencies (1 to 10 GHz), PHERMEX experiments also produce bursts of microwaves at gigahertz frequencies [Mack, Peratt, and Gisler 1987].

6.5.1 X Ray Emission

Moderately high atomic number plasma pinches with temperatures in the kilovolt range have been produced in discharges with megavolt electron energies and currents up to 5 MA. Figure 6.21 shows a typical experimental setup used to produce and measure X rays. One or more metallic or glass wires are strung between the cathode and anode of a pulse power generator diode (Figure 2.9). Typically, the wires have diameters of 15 μm, are 3 cm long, and are on a 20 mm array diameter. Streak and framing cameras and laser shadowgraphy follow the behavior of the plasmas produced when the ~100 ns pulse of energy explodes the wires into Bennett pinches. The self-consistent magnetic field is tens of megagauss in the 0.1–1 mm pinches.

If more than one wire is exploded, or if a jet of gas is injected between the cathode-anode gap, copious amounts of X ray radiation are produced. For example, neon (atomic number 10) produces ~55 kJ of K-line X rays at $h\nu \sim 1$ keV at frequency ν while titanium (atomic number 22) plasmas can produce ~10 kJ of K-line emission up to $h\nu \sim 10$ kJ. Figure 6.22 depicts the radiation energy as a function of the number of exploded wire filaments. As shown, an order of magnitude enhancement in X rays may be expected if at least two plasma filaments are present.

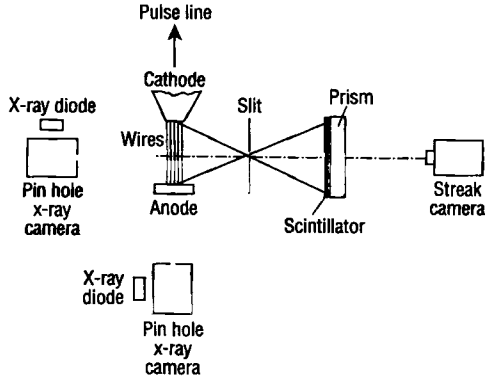

Figure 6.21. Experimental arrangement used to obtain X ray streak and frame photographs of the X ray source as it evolves in time. The X rays are imaged through a slit onto a strip of scintillator, which is then viewed by the streak camera through a prism (reference is made to Figures 2.9, 2.12, and 3.18).

6.5.2 X Ray Spectroscopy

X ray pinhole photographs and the spatial correlation of spectral emission show three types of emission emanating from exploded Z pinches. These are (a) hot-plasma thermal emission, (b) cool plasma thermal emission, and (c) nonthermal (synchrotron) emission.

The X ray emission from high-ionization states are recorded as narrow lines (using a curved crystal spectrograph [Rauch and Gersten 1982]) corresponding to the excited states of the elements present in the plasma. The high-temperature emission emanates from pinched regions along the plasma which emit X rays predominantly in the less than 3.5 keV energy region. Figure 6.23 shows the spectra produced by a titanium plasma.

Thermal X ray emission is also found from cooler-plasma regions with temperatures between 50 and 200 eV.

In addition to hot- and cool-plasma emission, X rays are also produced by relativistic electrons in the exploded-wire discharges. These X rays may have energies as high as ~8 keV and measurements of the shape and location of the radiating plasmas as a function of time show that the nonthermal X rays have time histories of longer duration than the pinches. The hard X ray emission produced by the energetic electrons generally begins about 20 ns after the beginning of the low energy X ray emission from pinches and lasts for the duration of the pulse discharge.

6.5.3 Morphology of the Thermal X Ray Source

Time integrated pinhole camera photography is used to acquire information on the size and shape of the radiating plasma. A pinhole camera may consist of a metal box containing the X ray film, with a number of pinholes covered by a graded aluminum foil material to increase the film latitude.

Figure 6.22. (opposite) (top) Radiated energy versus number of exploded wire filaments for a 1 MV, 1.3 MA pulse delivered to titanium wires. **(bottom)** Side-on X ray pinhole photograph of the plasma confined between the Bennett-pinched exploded wires (seen in absorption).

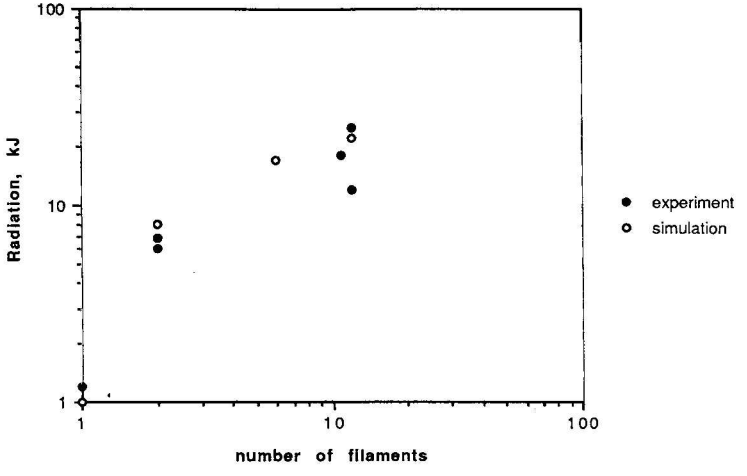
100
10
1
Radiation, kJ
1
10
100
number of filaments
experiment
simulation

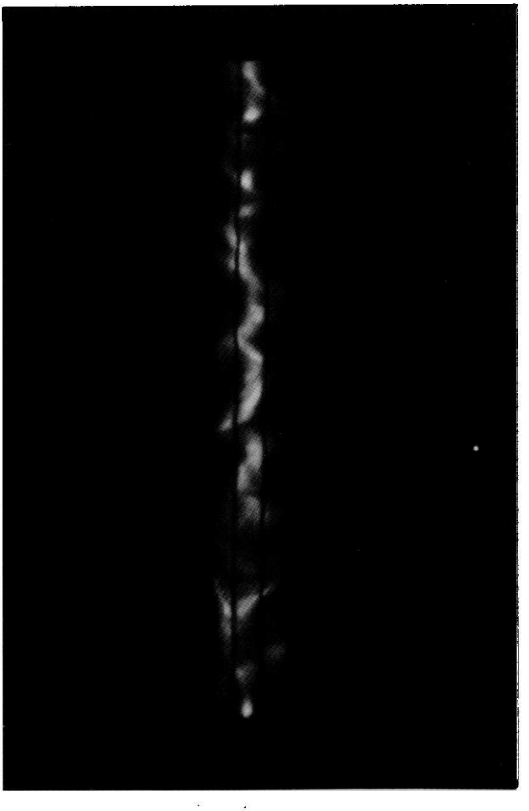

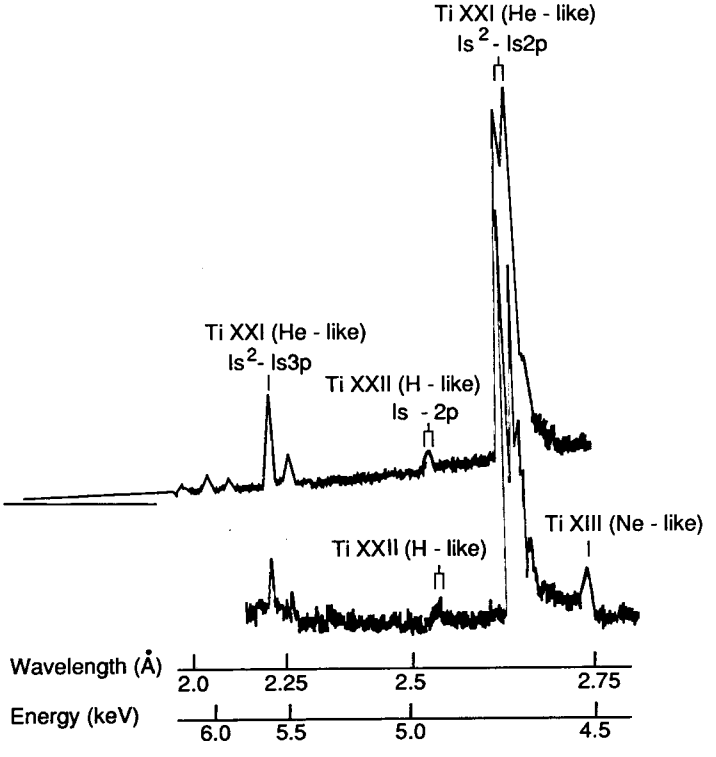

Figure 6.23. X ray spectra from titanium plasma (Figure 6.22) collected with a curved-crystal spectrograph.

A contour plot made from a pinhole photograph is shown in Figure 6.24 and shows that the intense X rays originate from hot spots along the plasma that is confined between the Bennett-pinched exploded wires.[1] The dimensions of the X ray hot spots are <100 μm in diameter; with cores often between 25 and 75 mm diameter. For a typical pinhole photograph with 5 hot spots of ~100 mm diameter emitting 10 kJ of X rays, the energy density per hot spot is 3.8×10^{15} J/m^3 (3.8×10^{16} ergs/cm^3), making the exploded wire the most copious energy density producer known of X rays from either laboratory or astrophysical plasmas.

The variability of the thermal X ray radiation, based on the "spikedness" of the XRD signal, is tens of picoseconds (i.e., corresponding to the speed of light dimensions of the emitting regions). The energy, of course, is supplied by the Marx bank via the transmission line (Figure 2.9), both of which are invisible in electromagnetic emission.

The plasma characteristics determined from the distribution of excitation states in the exploded-wire spectra corresponds well with those from other high-energy-density generating devices, namely, the vacuum spark and the plasma focus (Section 4.6.2).

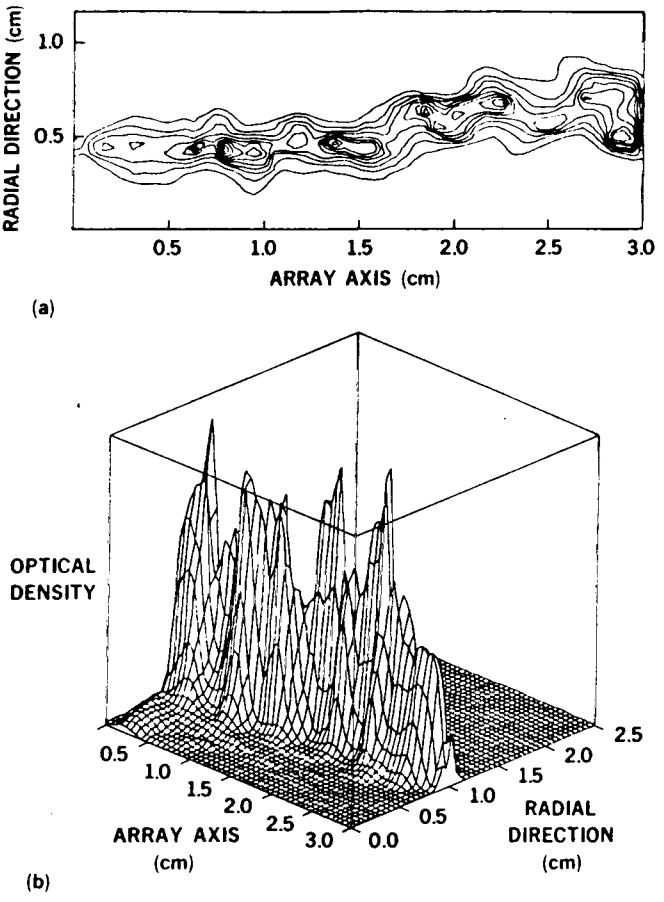

Figure 6.24. (a) Planar contour plot of a pinhole photograph from a titanium plasma. (b) Isometric plot of the optical density.

6.6 Particle-in-Cell Simulation of Synchrotron Processes

6.6.1 Simulated Z Pinches

Since I_z is often driven by a potential difference across a plasma column, an axial field component $\mathbf{E}_0 = \hat{\mathbf{z}} E_z$ may be present. Chapter 5 dealt with naturally occurring magnetic-field-aligned electric fields in current columns or filaments. Because of $\mathbf{E}_0$, the formulation given in the previous sections must be modified to include the acceleration of electrons parallel to $\mathbf{B}_0$. For this case $\dot{\boldsymbol{\beta}} = \dot{\boldsymbol{\beta}}_\perp + \dot{\boldsymbol{\beta}}_{\parallel}$, $\boldsymbol{\beta} \times \dot{\boldsymbol{\beta}} \neq 0$ [c.f. Eqs.(6.29) and (6.51)] and the equation of motion Eq.(1.5) is

$$\frac{d\,\mathbf{p}}{dt} = e\left(\mathbf{E}_0 + \mathbf{v} \times \mathbf{B}_0\right) \tag{6.97}$$

Because of the added complexity to the analysis of Sections 6.1–6.5, and because of geometrical complexities (Section 6.6.2), we choose instead to "brute-force" a solution via three-dimensional (three spatial dimensions), fully-electromagnetic (static and radiation fields), particle-in-cell simulations (Chapter 8).

6.6.2 Synchrotron Bursts from Simulated Z Pinches

An enhancement of radiated power Eq.(6.29) or Eq.(6.51) is achieved when the sum of the $\mathbf{v} \times \mathbf{B}$ radial forces seen by the relativistic electrons is increased, as is the case when the azimuthal magnetic fields of neighboring pinches are present (Figure 3.13). Whenever the attractive force between simulation columns causes their separation to be reduced to a distance such that the repulsive force Eq.(3.26) starts to become comparable to the attractive force Eq.(3.13), a burst in the radiation occurs (Figure 6.25). For the parameters used in these simulations, this distance is of the order of several pinch radii. As shown in Figure 6.25, the radiation from the kiloelectronvolt particles is polarized in the transverse plane and the synchrotron enhancement (burst) is detected in the x and y electric radiation energies (W_{ERx}, W_{ERy}) and the z magnetic radiation energy (W_{BRz}). The burst lasts until the induced axial magnetostatic energy W_{Bz}, due to the azimuthal current I_ϕ, is depleted [because the counterparallel azimuthal current force Eq.(3.26) brakes the azimuthal electron flow in both filaments]. For some simulation parameters, W_{Bz} can build-up and discharge again in the form of additional bursts of synchrotron radiation. The long-time, slowly varying increase in radiation in W_{ERx} and W_{ERy} is due to the buildup of electrostatic energy from charge separation in the particle number and size constrained simulation model.

The total power emitted as synchrotron radiation during the burst (simulation time T ~ 90) is

$$P^T = \frac{W^T_{rad}}{\tau_{burst}} \quad \text{AEU / time step} \tag{6.98}$$

where W^T_{rad} is the total radiated power in arbitrary energy units (AEU) and τ_{burst} is the burst duration in simulation time steps. Equation (6.98) may be converted to watts by scaling the simulation magnetostatic energy in AEU to a physical magnetostatic field in Tesla (the spatial dimensions and time in seconds are known quantities in a simulation):

$$P^T = \frac{W^T_{rad}\left[(2\mu_0)^{-1} B^2_\phi V / W_{ms}\right]}{\tau_{burst}\,(\text{seconds})} \quad \text{W} \tag{6.99}$$

Figure 6.25. (opposite) (a) Self-consistent axially-directed magnetic field vs time in dt' time steps. (b) and (c) Synchrotron radiation energy in the x and y electric field components, respectively. The ordinates are in arbitrary energy units (AEU).

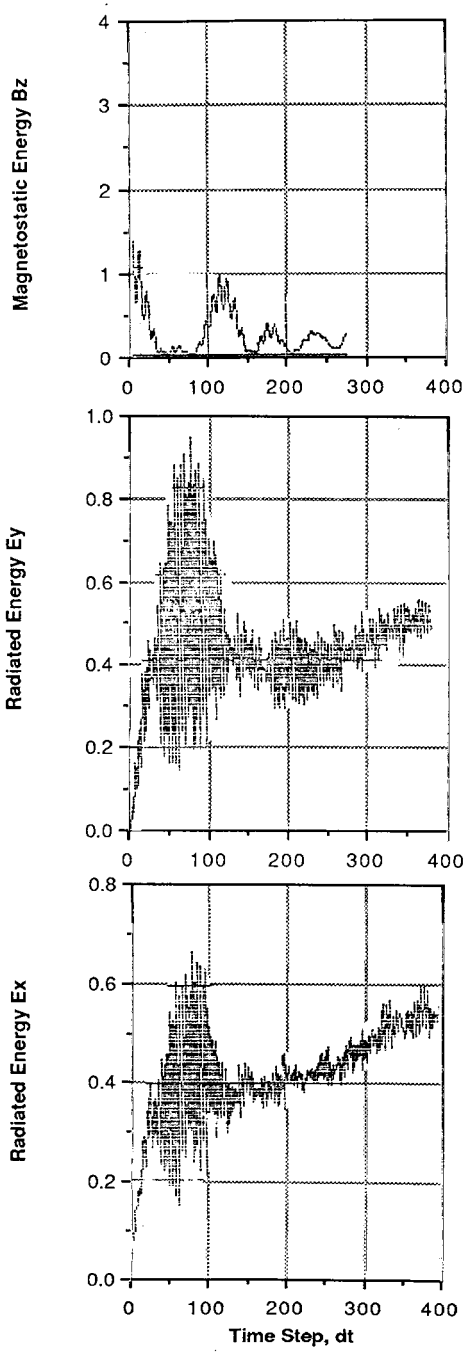
Magnetostatic Energy Bz
4
3
2
1
0
0
100
200
300
400
Radiated Energy Ey
1.0
0.8
0.6
0.4
0.2
0.0
0
100
200
300
400
Radiated Energy Ex
0.8
0.6
0.4
0.2
0.0
0
100
200
300
400
Time Step, dt

For this case, $W^T_{rad} = W_{ERx} + W_{ERy} + W_{ERz} = 2.1$ AEU and $W_{ms} = 350$ AEU. The radiation burst lasts ~ 20 dt' in the compressed simulation time frame (Section 8.6.3). Since time compression is achieved by using light ions, $m_i / m_e = 16$, the actual burst time in seconds is

$$\tau_{burst} = 20\, dt' \sqrt{1836/16} \tag{6.100}$$

Hence,

$$P^T = 2.8 \times 10^{-5} \frac{\left[B_\phi^2 V\right]}{2\,\mu_0\, dt'} \quad \text{W} \tag{6.101}$$

6.6.3 Synchrotron Source Radiation Patterns

When $\beta_{\parallel} > \beta_{\perp}$, interacting Z pinches beam a double-lobed radiation pattern in a direction close to $\mathbf{B}_0$. The basic shape is shown in Figures 3.13–3.17, which depict the magnetic isobars that confine the radiating electrons within the filaments. The isobars during the peak of the microwave burst are shown in Figure 6.26a. Because of the Biot–Savart forces between filaments, the currents in each filament have taken on a *C*–shaped cross-section from their original circular cross-sections. The most intense currents are confined to narrow regions within the *C*–shaped lobes. These are shown as spots in Figure 6.26a, which are found to be diagonally juxtapositioned in the two lobes. This juxtaposition marks the start of the rotation of filaments (Figure 3.14).

The two lobes represent regions of strong synchrotron emission while the radiation is most intense from the spots within the lobes.

Examples of isophotes of the generated electric field strength (squared) $|\mathbf{E}|^2$ over a time span which includes the microwave burst are shown in Figure 6.27a. These isophotes show where the acceleration fields are strongest, and therefore depict the radiation patterns of the forward-beamed synchrotron emission [c.f. Eq.(6.57)]. As shown, the $|\mathbf{E}|^2$ isophotes tend to be more complex than the $|\mathbf{B}|^2$ isophotes and often show additional filamentation in each radiating lobe. At early times, before and during the microwave burst, the acceleration fields tend to be strongest at the outer edges of the lobes. At later times, $|\mathbf{E}|^2$ maxima migrate inward within the filaments, eventually producing a "butterfly" like radiation pattern. The fourth frame of Figure 6.27 shows the vectors $\mathbf{B}$ overlaid on $|\mathbf{E}|^2$, giving information on the polarization properties of the radiation from the filaments. In general, the $\mathbf{B}$ vectors are maximum where they lie transverse to $|\mathbf{E}|^2$.

6.7 Synchrotron Radiation from Cosmic Sources

6.7.1 Gross Radio Properties of Galaxies

Most cosmological objects, including galaxies, are emitters of synchrotron radiation, over a relatively wide band encompassing radio frequencies through optical frequencies. The radio power L of galaxies, integrated from 10 MHz to 100 GHz, ranges from about 10^{30} W to about 10^{38} W, and relative to their optical luminosity, from less than 10^{-6} to about 1 [Perola 1981]. The

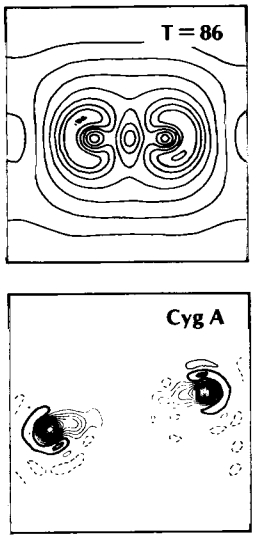

Figure 6.26. **(top)** Magnetic energy isobars B^2 in the plane perpendicular to the axial field-aligned currents at time of peak burst of synchrotron radiation. The most intense fields are the "hot spots" in the radiation lobes. A B^2 minima exists between the two outflowing currents. **(bottom)** Isophotal contours of synchrotron radiation at 150 MHz from Cyg A. An elliptical galaxy is situated midway between the two radio lobes.

distribution in power is described by means of the *Radio Luminosity Function* (RLF) which represents the number of radio emitting galaxies per unit volume as a function of the monochromatic power at a certain frequency. Figure 6.28 illustrates the RLF at 1.4 GHz at the present cosmological epoch, the "local" RLF.

The RLF suggests a continuity in the morphological types of radioemitting galaxies. Above 10^{26} W/Hz, the main contribution comes from quasars and classical double radio galaxies. In the region 10^{23}–10^{26} W/Hz, the elliptical galaxies dominate while below 10^{23} W/Hz (about an order of magnitude greater than the power of our Galaxy) the power comes principally from spiral galaxies.

In the region 10^{21}–10^{23} W/Hz, an overlap of spiral and elliptical galaxies occurs. The "ellipticals" are in fact a hybrid class, containing bona fide ellipticals along with *N* galaxies (a bright nucleus surrounded by a faint nebulosity) to that of *cD* galaxies (giant ellipticals with very extended radio "halos"). Noteworthy in Figure 6.28 is a "break" in synchrotron power from ellipticals at $10^{24.5}$ W/Hz and another at $10^{21.3}$ W/Hz for spirals.

The size of the radioemitting regions in galaxies spans a very wide range. At powers larger than about 10^{23} W/Hz at 1.4 GHz the radio emission is generally dominated by an extended component, whose size goes from tens of kiloparsecs (e.g., Cygnus A) to tens of megaparsecs (e.g., 3C236). Often a very compact central radio component is present, whose power ranges from 10^{22} up to 10^{25} W/Hz, and which may be seen to vary with time. Extended and central radio components are typically found also in quasars.

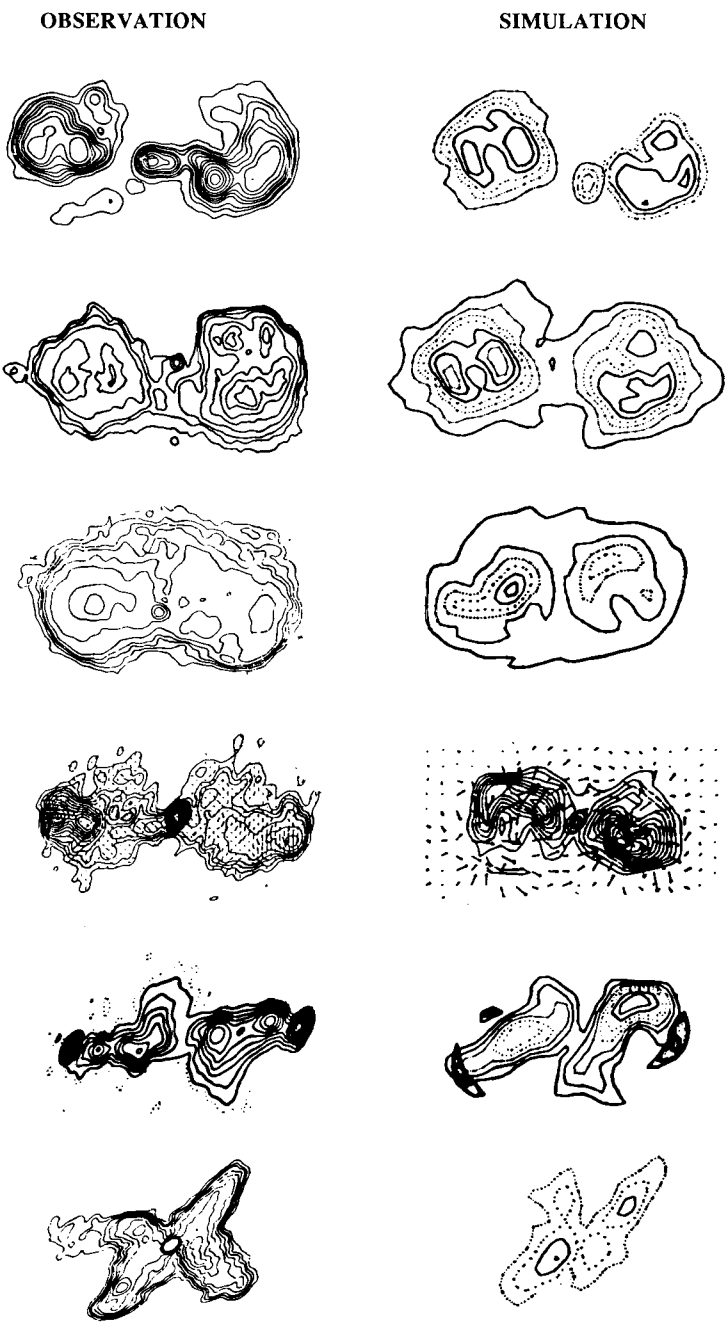

Figure 6.27. (right) Electric energy isophotes E^2. Top to bottom: simulation times $T = 51, 52, 236, 237, 280,$ and 288 dt', respectively. **(left)** Synchrotron isophotes (various frequencies) of double radio galaxies and quasars. Top to bottom: 0844+319, Fornax A, 3C310, 2355+490, 3C192, and 3C315.

Table 6.1. General properties of galactic radio sources

Source type	power, W/Hz	geometry and dimension	redshift, z
quasars, double radio galaxies	10^{26}-10^{29}	two extended radio lobes separated tens of kpc to Mpc; oftentimes a central component is present	0.3-3.8 0.01-1.8
elliptical galaxies:	10^{23}-10^{26}	kiloparsecs to decaparsecs, devoid of any magnetic field	
cD		giant ellipticals with very extended haloes	~1
N		bright nucleus surrounded by faint nebulosity	
	$10^{24.5}$	break in RLF	
	10^{26}	Seyfert-like spectra	
Seyfert spiral galaxies		elementary spirals of a few tens of kpc extent; most active nuclei	0.01-0.09
spiral galaxies	$<10^{23}$	two radio components coincident with spiral disk, kpc-sized nuclear region	0.003-0.5[a]
	$10^{21.3}$	break in RLF	

[a] Andromeda is blueshifted

At powers less than about 10^{23} W/Hz, the size of the radio region in elliptical galaxies is generally measured in kiloparsecs and often reduces to a compact central component. In spiral galaxies, the next stage of a suggested epochological sequence in Figure 6.28, the situation is different. Apart from the radical change in morphology between elliptical and spiral, the spiral galaxies not only have a compact nuclear component (of radio dimension between 0.1 and 1 kpc) but also a component of size ~10 kpc, coincident with the spiral disk.

Overlapping the powerful radio ellipticals (with Seyfert-like nuclear spectra) and spiral galaxies are the Seyfert-spirals themselves, comprising 1% of all spiral types. In contrast to the ellipticals, spiral galaxies rarely have compact nuclear sources and are unassociated with extended radio lobes. Table 6.1 delineates the properties of galactic radio sources.

Figure 6.29 shows the positions of the radio sources, both extended and compact on a linear-size, radio-luminosity plot. As seen, the bulk of the classical double radio galaxies possessing an elliptical galaxy have a spatial extent between a few tens of kiloparsecs to many hundreds of kiloparsecs, with radio luminosities of L~10^{35} to 10^{39} W. Some transitional radiogalaxies, 8–80 kpc, and L~10^{34} W, are also present. The radioquasars appear in two distinct populations; extended sources with dimensions of several kiloparsecs to several hundreds of kiloparsecs (L~10^{37}–10^{39}

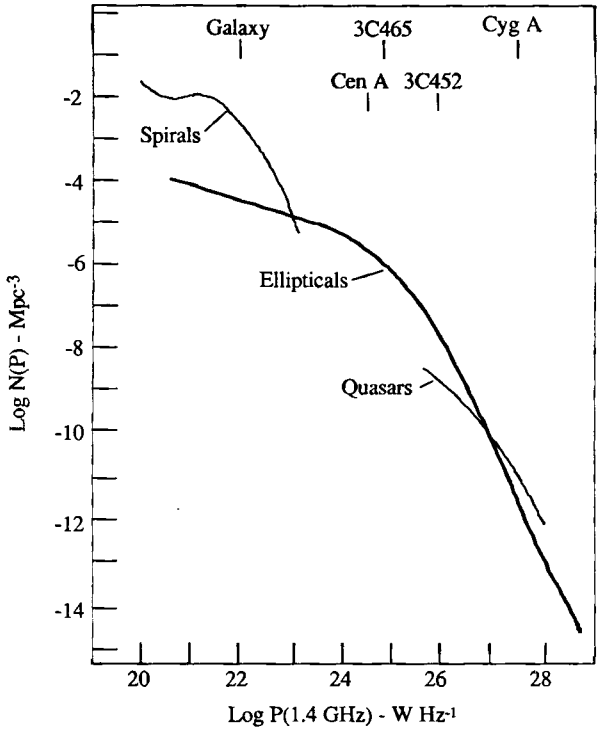

Figure 6.28. The radio lumninosity function of galaxies and quasars (adapted from Fanti and Perola, 1977).

W), and compact sources ~2 to 8 parsecs (L~10^{37}–10^{39} W). Most of the spiral galaxies are found to be clustered according to a size-luminosity of ~10–80 kpc, and L ~10^{31}–$10^{32.5}$ W.

Finally, unlike their other properties, the radio spectra of the spiral galaxies are similar to those of the radio galaxies. The nuclear component of our galaxy, for example, is a miniature replication of a classic double radio galaxy (Figure 3.23).

6.7.2 Double Radio Galaxies

The discovery of discrete radio sources dates back to the pioneering survey of Reber (1944), who found areas of enhanced radio intensity in the constellations Cygnus and Cassiopeia. Many excellent reviews of double radio sources are available in the literature [Shklovksy 1960, Pachoczyk 1977, Miley 1980, Perola 1981], as are a number of models of sources. However, regardless of whatever ingredients are postulated as necessary in models used to "explain" their existence, what is observed from any radio source is synchrotron radiation, that requires only relativistic electrons in the presence of a magnetic field.

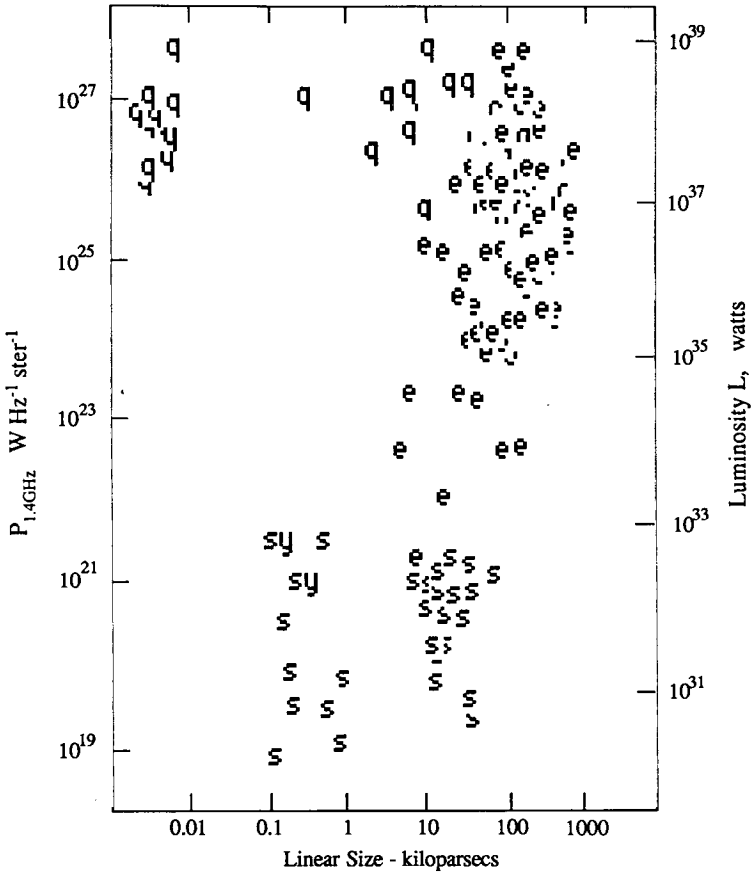

Figure 6.29. Plot of the monochromatic radio power at 1.4 GHz versus linear size for classes of extragalactic radio sources. The symbol *e* denotes extended radio sources associated with an elliptical galaxy core while *q*, *sy*, and *s* denote quasars, Seyferts, and spiral galaxies, respectively (adapted from Eckers, 1974).

One of the first low-resolution radio maps made of a radio galaxy was the strong source Fornax A (Figure 6.30). The pattern depicted in this figure is that of two radio emitting regions (thus giving "double" radio galaxies their name) situated on either side of an elliptical galaxy (NGC 1316). Improvements in radio telescope technology led to higher resolution maps such as that of Cygnus A shown in Figure 6.26b. Cygnus A, the brightest radio source in Cygnus, has proved to be the "prototype" of double radio galaxies and models of double radio galaxies are usually based on the characteristics of this source. As shown in Figure 6.26b, Cygnus A consists primarily of two radio lobes of dimension $l \cong w \cong 35$ kpc (10^{21} m) separated on either side of an elliptical galaxy by a distance $a \cong 80$ kpc (1.22×10^{21} m). Cygnus A is thought to be characterized

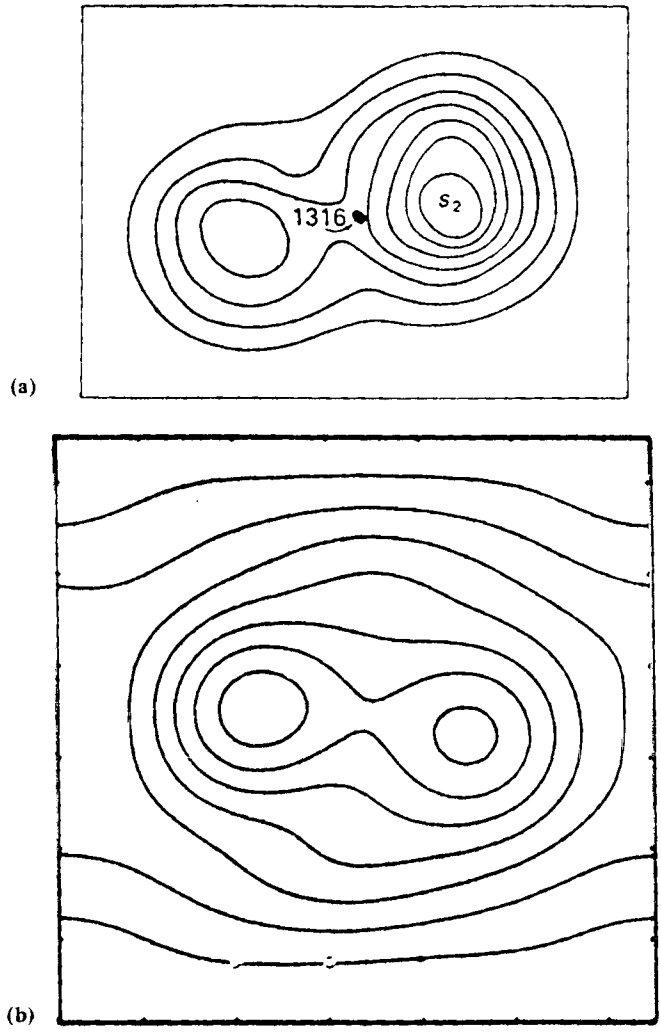

Figure 6.30. **(a)** Low resolution intensity contours of the double radio galaxy Fornax A. The peculiar galaxy NGC 1316 is shown between the radio lobes. **(b)** Low resolution magnetic isobars of interacting Birkeland currents during synchrotron burst era.

by the parameters $B \sim 10^{-9}$–10^{-7} T (10^{-5}–10^{-3} G), $T \sim$ 1–10 keV, $n_e \sim 10^2$–10^4 m^{-3} (10^{-4}–10^{-2} cm^{-3}), $L \sim 1.6$–4.4×10^{37} W, with a total source energy of 10^{50}–10^{57} J. The average energy of the relativistic electrons is estimated to be 100–158 Mev [Sturrock 1969, Perola 1981].

Example 6.3. Double radio galaxy simulation model and parameters. To simulate a radio galaxy, the results of Section 6.6.2 are used and the simulation geometry is that shown in Figure 3.12 scaled to double radio galaxy dimensions (the reason for two filaments is discussed in Section 3.10.6). In analogy to Cygnus A, the two filaments are taken to have a width of 35 kpc with a separation of 80 kpc. Assuming that the total plasma mass M over a length L (~10^{21} m) of filament involved in Biot–Savart attraction is of the order of that observed in Galaxies, $M \cong 10^{41}$ kg, while setting the velocity between galactic filaments to 1,000 km/s [Peratt and Green 1983] in (3.49), yields $I_z \cong 2.15 \times 10^{19}$ A and $B_\phi = \mu_0 I_z / w \cong 2.5 \times 10^{-8}$ T (2.5×10^{-4} G). (The quantities I_z and B_ϕ are physically nonsensitive to the actual mass distribution, depending only on the square-root of the mass per unit length).

To convert simulation results to dimensional form, it is sufficient to fix the value of one physical quantity (e.g., B_ϕ). Since we are scaling to the strong radio source Cygnus A, the value of B_ϕ is applied at time step 90 in Figure 6.25, the peak of the synchrotron burst energy. At this time the simulation shows that B_ϕ has grown comparable in strength to B_{z0} so that the pressure ratio has decreased to about β_p=0.0034 from the setup values of Section 3.10.1. For $B_\phi = 2.5 \times 10^{-8}$ T, the magnetostatic energy Eq.(6.99) $W_{ms} = 350$ AEU $= 2.5 \times 10^{53}$ J, or 1 AEU $= 7.1 \times 10^{50}$ J.

Counting and plotting the thermal velocities of the electrons at time $T = 90$ shows a Maxwellian velocity distribution with a corresponding temperature $T_\perp \approx 2.8$ keV. Substituting β_p, $T_\perp$, and B into Eq.(8.20) yields a mean plasma density $n_e = 1.79 \times 10^3$ m^{-3} (1.7×10^{-3} cm^{-3}). Since $\omega_{c0}/\omega_p = 1.5$ (Section 3.10.1), the axial magnetic field strength is $B_{z0} = 2.0 \times 10^{-8}$ T (2.0×10^{-4} G). These parameter values characterize Cygnus A and are in close agreement with many previous estimates using independent means. Additionally, from the simulation parameter E_{z0}/B_{z0}=0.002c, the acceleration field within a filament is $E_{z0} = 12$ mV/m.

To scale the simulation spatial and temporal setup dimensions, $\Delta = 4\lambda_D = 2.97 \times 10^4$ m and $dt = (4\omega_p)^{-1} = 1.04 \times 10^{-4}$s, to Cygnus A requires a size/time multiplication factor Eq.(8.21) of $\alpha = 5.6 \times 10^{15}$, so that $3\Delta' = 35$ kpc. Hence, $\Delta' = \alpha\Delta = 1.66 \times 10^{20}$m and $dt' = \alpha\, dt = 5.87 \times 10^{11}$s are the galactic equivalent cell and time step, respectively.

Example 6.4 Radiated power from a simulated double radio galaxy. An estimate of the total power emitted as synchrotron radiation follows directly from the results of Section 6.6.2. From Figure 3.15, B_ϕ is seen to be largely constrained to the volume of the plasma filaments so that $V_p \sim (10^{21}\text{ m})^3 = 10^{63}$ m^3. Substituting B_ϕ, V_p, and dt' into Eq.(6.101) gives a total power emitted in synchrotron radiation of 1.16×10^{37} W, which is to be compared with the radio luminosity of Cyg A of 1.6–4.4 $\times 10^{37}$ W. Table 6.2 compares the simulation and estimated parameters for Cyg A. The agreement between the model predictions and the estimated parameters are generally quite good. For comparison purposes, the synchrotron isophotes of several radio galaxies and quasars are arrayed against their simulation counterparts in Figure 6.27.

Example 6.5. Synchrotron spectrum. The total kinetic energy of the electrons during burst is $W_{KE} = 8.78 \times 10^4$ AEU $= 6.26 \times 10^{55}$ J. The total number of electrons is $N = n_e V_p = 1.79 \times 10^{66}$, so that the average kinetic energy per electron is $\overline{W} = 218$ MeV (1 Joule $= 6.242 \times 10^{18}$ eV).

The most probable energy associated with the electron energy distribution is $W_0 = 2/3\ \overline{W} =$ 145 MeV and, based upon the velocity distribution of the simulation superparticles, the electron energies range from 20.3 to 406.5 MeV [Peratt and Green 1983]. The critical frequencies associated with these energy bounds Eq.(6.70) are 1.35 and 541 MHz, respectively. The total incoher-

Table 6.2. Comparison of simulation and estimated radio galaxy parameters

Parameter	Simulation value (Cygnus A)	Estimate (model/object dependent)	Author[a]
Galactic current, I_z, A	2.15×10^{19}	10^{17}-10^{19}	Alfvén (1981)
Galactic magnetic field, G	2.5×10^{-4} (B_ϕ)	10^{-5}	Perley *et al* (1979)
	2.0×10^{-4} (B_z)	3.16×10^{-4}	Mills and Sturrock (1970)
		3×10^{-4}	de Young and Axford (1967)
		1.2×10^{-4}	Hargrave and Ryle (1974)
		10^{-5}-10^{-3}	Perola (1981)
Plasma temperature, $T_\perp$, keV	2.8	1-10	Miley (1980)
		10	Gisler and Miley (1979)
Plasma density, n_e, cm^{-3}	1.79×10^{-3}	4×10^{-3}-2×10^{-2}	Perley *et al* (1979)
		10^{-4}-10^{-3}	Miley (1980)
		0.6×10^{-3}	Gisler and Miley (1979)
density of synchrotron emitting electrons, n_e^{syn} cm^{-3}	6.9×10^{-9}	10^{-9}	Shklovsky (1960)
		1.5×10^{-8}	Ginzburg and Syrovatskii (1965)
P_{syn}, W	1.16×10^{37}	1.6×10^{37}	Moffet (1975)
		4.4×10^{37}	Shklovsky (1960)
t_{syn}, yr	4×10^6	10^4-4×10^6	Sturrock and Barnes (1972)
		$>3\times10^7$	de Young and Axford (1967)
		5×10^6	Ryle and Windram (1968)
Total source energy, J	6.3×10^{55}	10^{57}	Sturrock and Barnes (1972)
		$>10^{54}$	de Young and Axford (1967)
Average energy per electron, $T_{\|\|}$, MeV	218	>100	Perola (1981)
		158	Sturrock (1969)

[a]Adapted from A. Peratt (1986)

ent spectrum follows from Eq.(6.71) and is shown in Figure 6.31 (solid line). This curve is a superposition of the individual electron spectra and includes the contribution of each spectra to ten times its critical frequency.

This spectrum may be directly compared to the spectrum of Cygnus A as compiled from a number of independent flux-frequency measurements as shown in Figure 6.31 (crosses) [Mitton and Ryle 1969]. Beyond 1 GHz, the fall-off on the simulation spectrum is due to the neglect of a smaller number of higher energy, run-away, electrons. The run-away electrons can attain energies as high as 3×10^{17} eV over an axial distance of 10 kpc with a millivolt per meter electric field.

6.7.3 "Jets" and Superluminosity

The term *jet* was first used in astrophysics by Curtis [1918] to describe an elongated optical feature protruding from the core of the elliptical galaxy M87. Later Baade and Minkowski [1954] sug-

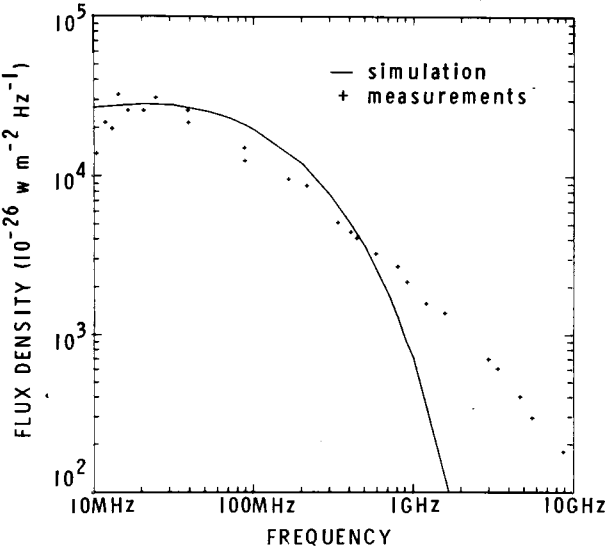

Figure 6.31. The radio spectrum of Cygnus A. The absolute results of the electromagnetic particle simulations and measurements are shown.

gested that such a jet might actually correspond to matter ejection after some active phase of the core. Jets have been mapped in about 200 radio sources. Jets are found not only in double radio galaxies and quasars, but also in central compact radio sources located in the nucleus of associated (optical) galaxies. They are measured from the synchrotron radiation they emit, from centimeter wavelengths to X rays. However, in spite of improved resolution and statistics of observations, definitive direct evidence that ordered streaming motions are present in jets or radiosources is still missing. Moreover, uncertainty exists in identifying structures as either "jets" or "bridges."

Figure 6.32 shows VLA observations of radio quasars having jets (7 out of 26 quasars in a 966 MHz Jodrell Bank survey) and three quasars with faint jets. The general morphology is that of a filamented structure in emission that is connected to a core located midway between two strong radio lobes.

Comparison of the integrated magnitude of the jet in M87 over the period 1934–1980 shows that the jet is variable and has been fading, more or less uniformly, by about 0.8 mag per decade between 1964 and 1980. The data imply that over the period 1952-1980, the total jet intensity fell by at least 2.5 mag. Comparisons of isophotes taken in 1964 and 1979 show no obvious differences in overall shape, apart from effects of variation and noise. This indicates that the fading has affected the whole channel uniformly since 1964 [i.e., the "knots" or hot spots in the jet (Figure 6.33a,b,c) have not been seen to move]. However, between 1934 and 1956, knots A and B became significantly brighter than C.

At a distance of 11.4 Mpc, the channel length of M87 is 30 arcsec in the plane of the sky, or 5,400 light years across. For this reason, and because side-on photographs of charged particle

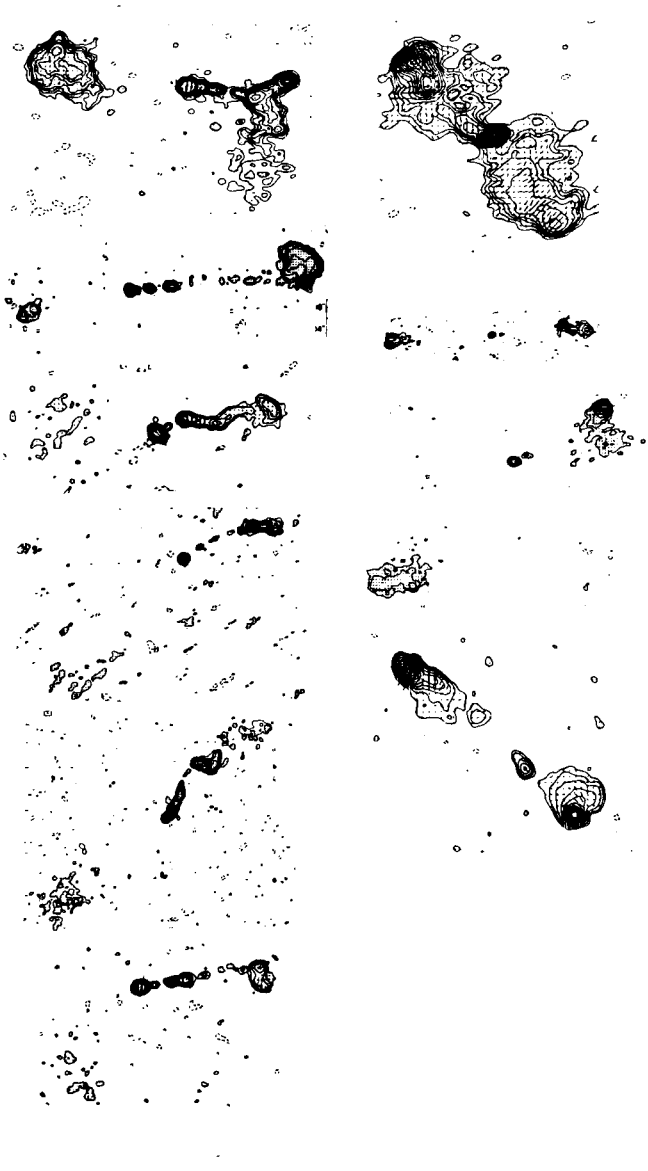

Figure 6.32. Ten examples of Very Large Array observations of radio quasars having jets. the general morphology is that of a filamented structure in emission that is connected to a core located midway between two strong radio emitting plasmas. The bottom three sources in the right-hand column are designated as "faint" jets.

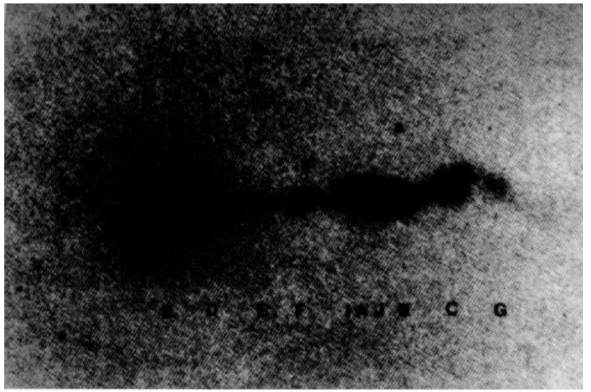

(a)

REB (d)

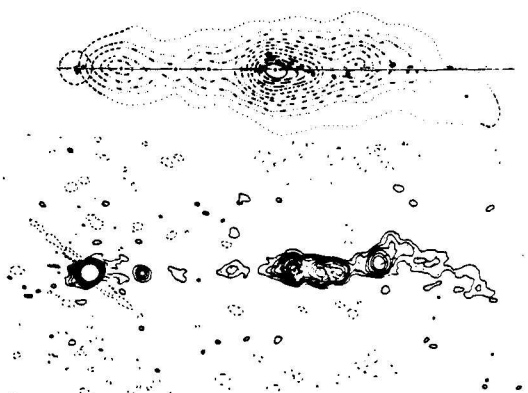

(b)

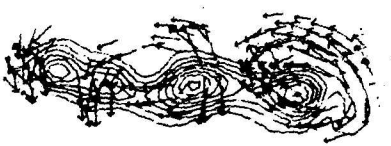

B^2, B (e)

(c)

Figure 6.33. **(a)** Optical synchrotron radiation from the "jet" in M87. **(b)** Isophotes and projected magnetic field vectors. **(c)** "Knots" within the jet. **(d)** Relativistic electrons in a jet simulation (the sheet beam electrons are inductively accelerated out of the plane of the page). **(e)** Magnetic energy contours and vectors from simulation.

beams display different morphologies, the explanation of observable jet fading based on side ejected matter models is untenable.

Example 6.6 Simulated emission bridges between radio lobes and core. Plasma confined in the core and channel connecting one of the current filaments by magnetic isobars has been discussed in Section 3.10.4. Using the scaling of Example 6.3, the length of the channel is $9\Delta' = 1.5 \times 10^{21}$ m (49.8 kpc) while the width varies from about $0.5\Delta'$ (2.8 kpc) to $2\Delta'$ (11 kpc). At time T =255 (1.6×10^{15} s or 51 Myr), the confining field B_ϕ (from Figure 3.17) is 2–2.5 $\times 10^{-8}$ T, so that the pressure [Eq.(3.51)] is 2.5×10^{-9} Pa, allowing the confinement of a 10^9 m^{-3} (10^3 cm^{-3}) 2 eV plasma. The inwards magnetobaric velocity Eq.(3.52) is 8,990 km/s, about 9 times faster than the Biot–Savart attraction velocity between synchrotron radiating filaments. Through Eq.(1.1), the time varying B_ϕ produces an axial E_z field within the plasma, accelerating the electrons in one direction and the ions in the other. Figure 6.34 shows the induced electric field variation at the mid-sections of the two filaments (the radio lobes), the core, and within the channel on either side of the core [Peratt 1986]. From top to bottom, the most intense electric field activity occurs earlier in the outer filaments at time $T \sim 180$–270, then later at time $T \sim 320$–390 in the core. Whether or not an observer can see synchrotron radiation depends on his orientation with respect to the polarity of the electric field. A positive value for E_z accelerates electrons in the $-z$ direction, which is also the direction of the gain pattern Eq.(6.57). An observer in the $+z$ direction, or out of the gain pattern, would observe radiation only from the thermal plasma, which may be the case for some radio quiet quasars.

The rapid spatial variation of the induction field, as well as the changing field polarity along the channel, causes an apparent "superluminosity" effect as the field sweeps the channel confined plasma. Figure 6.33d,e shows the simulated plasma and its magnetic field. Rather then being core ejected material, the simulated "jet" is a sheet electron beam (Section 2.7.1) accelerating out of the plane of the page.

6.7.4 Quasars and Active Galaxy Nuclei

Quasars can be delineated into two classes, radio quasars and radio-quiet quasars (Figure 6.29). However, there is little to distinguish between a double radio galaxy and a radio quasar. In a redshift range 0.1–0.5, both are found in equal numbers with matched radio luminosities and spectral indices. The quasars appear to be the larger radio sources with strong cores of flat spectral index; the strongest radio lobe sources are radio galaxies. Hutchings (1987) finds that nearly 70% of the radio quasars and over 80% of the radio galaxies are interacting objects, the median separation being 20 kpc for quasars and 12 kpc for radio galaxies. From this he infers a relative velocity of 1,000 km/s (identical to the value determined in Example 6.3) and deduces an upper limit of 10^8 yr for radio activity [Eq.(6.100) yields 4×10^6 yr]. Approximately 30% of all objects have an elliptical, or a disturbed elliptical galaxy located between the radio lobes; none has spiral. The median source size for the radio quasars is 104 kpc compared to 60 kpc for radio galaxies.

There is a major difference between the radio quasars and the double radio galaxies: Quasars all have strong nuclear cores while radio galaxies all have very weak cores.

Radio quiet quasars lack the double lobe radio structure but retain the characteristic core signatures: emission lines of hydrogen and other light elements. In addition, unlike radio quiet quasars, radio quasars often have a compact radio component coinciding with the core. Radio

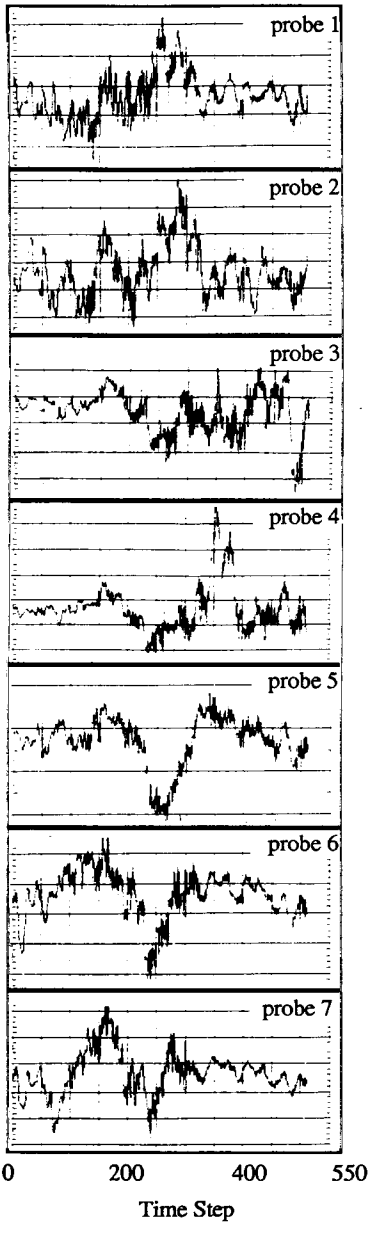

Figure 6.34. Induction electric field E_z from field probes indicated in Figure 3.17.

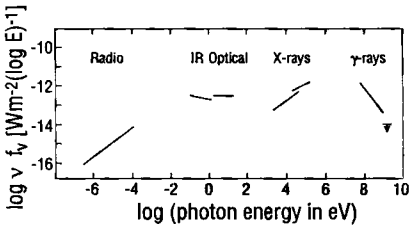

Figure 6.35. The continuum spectrum of the quasar 3C273 plotted as νF_ν against frequency ν in electronvolts.

variability is shown by this component, in the same way as the quasar varies optically. The time-scales of the variability for the optical and core radio components are of the order of one year.

The optical spectra of quasars are similar to those of Seyfert galaxies. Both are strong infrared emitters, but quasars are intense emitters at X ray and gamma wavelengths (Figure 6.35). For example, NGC 4151 (Figure 3.27b), the brightest of Seyfert galaxies, shows strong emission lines of hydrogen, helium, carbon, and magnesium. The short wavelength continuum of NGC 4151s spectrum indicates a temperature of about 3 eV. The variability of the lines and the continuum varies greatly on time scales from days to months. From the point of view of spectroscopy, quasars cannot be distinguished from Seyfert galaxies. The continuity in spectra for a quasar, Seyfert, narrow emission line galaxy, and a normal spiral galaxy is shown in Figure 6.36.

Example 6.7. Simulated quasar evolution. Figures 3.15 and 3.19 (morphology evolution), Figure 6.25 (temporal characteristic of synchrotron radiation), and Figure 6.34 (time-space history of the accelerating field E_z) allows the study of the morphological and radiation history of a simulated quasar. At early time (5–10 Myr) in the interaction of two current-carrying filaments (scaled to the parameters of Example 6.3) only synchrotron radiation from the two sources (precisely, the cross-sections of the interacting filaments where the double-layer E_z field occurs) can be seen in the gain pattern. At about 20 Myr, the intensity reaches some 10^{37} W while diffuse inter-filament plasma has been collected into the elliptical core and channel regions. The plasma in the channel can radiate via the synchrotron mechanism (Example 6.6), albeit a much lower intensity than the outer sources. The thermal plasma compressed into the core, in analogy to Section 6.5.2, might be expected to also display a two-temperature spectral profile: a continuum and excitation lines of light elements. After ~50 Myr, the synchrotron burst era comes to a close with a fall in the intensity of radiation from the filament sources. In spite of this, the current conducted by the filaments continues to increase from 2×10^{19} to 4×10^{20} A (because of the constant E_z). This compresses the plasma in the core and reduces its dimension from about 50 kpc in extent to 10 kpc or less at much later time. The heated core plasma is eventually enveloped by the source plasmas which spiral inward to mimic the morphology of a Seyfert galaxy (Figure 3.27a). The two original hot spots which marked the most intense regions of axial current flow and which are the sources of synchrotron radiation, now reside within the core of the galaxy.

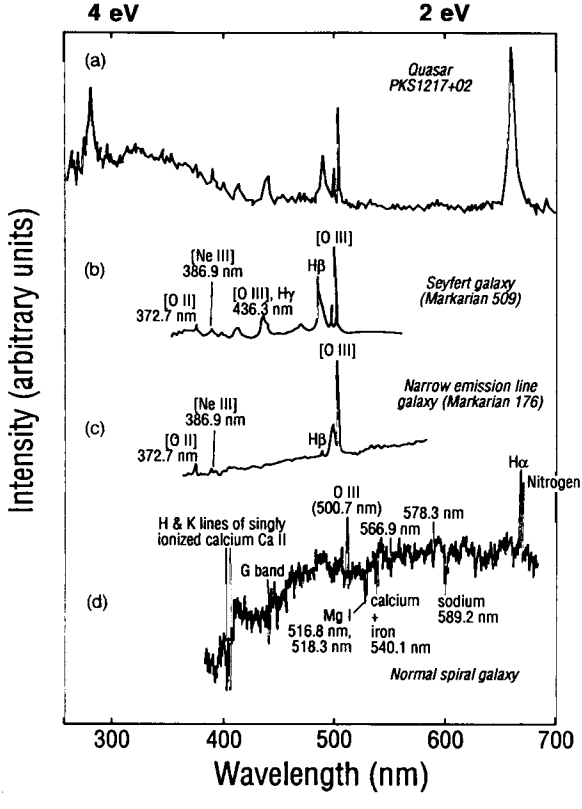

Figure 6.36. **(a)** Spectra of the nearby (z=0.2) quasar PKS 1217+02. **(b)** Spectra of the Seyfert galaxy Markarian 509. This spectra is similiar in all respects to (a). The Balmer lines Hβ, Hγ are very wide while the forbidden lines such as [OIII] are narrow and are comparable to the Hα line in a normal spiral galaxy. **(c)** Spectra of the narrow-emission line galaxy Markarian 176. Compared to Seyferts, this class of galaxy does not have active nuclei. **(d)** Spectra of a normal spiral galaxy. Spectra are plotted versus wavelength, nm (bottom), and energy, eV (top).

6.7.5 X Ray and Gamma-Ray Sources

Figure 6.37 plots the luminosity L and magnetic field B versus frequency ν in keV for a number of classes of astrophysical objects having both steady and "burst" emissions. Liang (1989) has pointed out the suggestive trend linking the so-called classical gamma ray bursters with two other impulsive phenomena, namely, the aurora from geomagnetic storms (Section 2.9.8) and impulsive solar X ray flares (Section 5.6.2). Like the aurora and solar flares, X ray and gamma ray sources are likely to have their radiative energies supplied by electrical currents (Section 6.5).

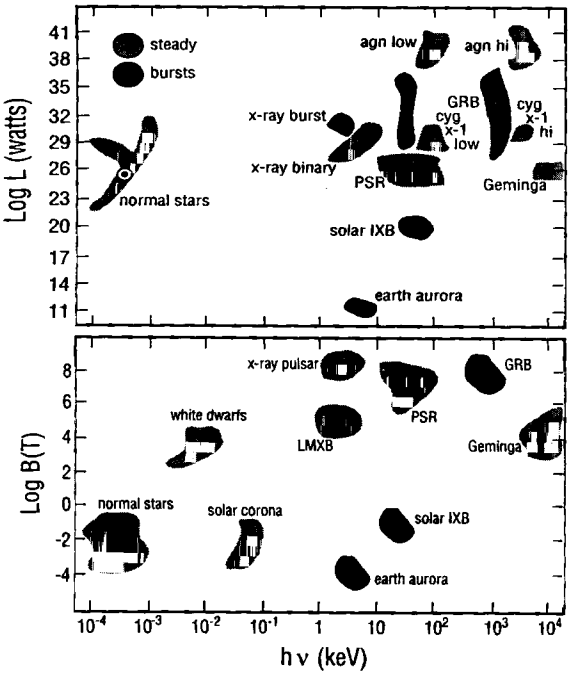

Figure 6.37. The location of various classes of steady and burst astrophysical sources in luminosity L and magnetic field B versus frequency ν in keV (adapted from Liang, 1989).

Notes

[1] The "island universes" concept was introduced by the philosopher Kant (1724–1804).

[2] A time frame study of the fields shows that the strength of the "static" component does vary slowly in time.

[3] The function $\delta(y)$ is to be interpreted as $\delta(y)T/2\pi$ where T is the period of revolution.

[4] While $P_{\omega}^{(0)}$ has no rotation, $P_{\omega}^{(1)}$ does rotate.

[5] Long after the thermal plasma X ray burst, streak photographs show the Bennett-pinched exploded wire plasmas converging onto the centrally confined plasma because of the Biot-Savart attraction. The pinhole camera placed in front of the anode records a single "dot" of X rays.